University of Glasgow

MARK MAIN

2397001M

TOWARDS QUANTITATIVE OPTICAL STRATEGIES FOR MEASURING BLOOD REPERFUSION IN MICROFLUIDIC ANALOGIES

James Watt School of Engineering

MEng in Electronics & Electrical Engineering

Project ENG 5041P

Academic Year: 2022-23

Supervisor: Dr Akhil Kallepalli, Prof Hadi Heidari

University of Glasgow

James Watt School of Engineering

MEng in Electronics & Electrical Engineering

Academic Year: 2022-23

MARK MAIN

Towards quantitative optical strategies for measuring blood reperfusion in microfluidic analogies

Supervisors: Dr Akhil Kallepalli, Prof Hadi Heidari

ABSTRACT

In post-operative care following skin transplant, there are several key metrics that must be monitored to determine the long-term viability of the tissue. One of the primary factors observed during post-operative assessments is reperfusion of the tissue, i.e., reintroduction of blood within the tissue and the quality of the flow itself. Currently, this assessment is a qualitative procedure in which medical personnel physically compress and release the tissue to observe colour changes that present themselves as a result of capillary refill, amongst other methods. The combination of human error, anatomical variations and environmental factors makes this method unreliable and increases the likelihood of short-term tissue failure. Using visible and shortwave infrared wavelengths of light in a non-contact approach, a proof-of-concept undertaking is investigated for a safe and accurate solution.

In this thesis, the viability of optical wavelengths and optical windows of transmission is assessed for quantitative perfusion monitoring. This is achieved through both simulations, based on light transport through a human forearm, and experimental proof of concept using a homodyne measurement system. The simulations build upon earlier work (Main *et al.* 2022), by exploring the variation of optical scattering during hypertensive episodes (high blood pressure due to vessel wall thickening). By conducting these simulations, a measurable change in overall scattering due to changes in blood vessel geometry is observed. This presents the mandate to develop an experimental system to test this in living tissue.

Experimentally, two approaches were tested; the first method explored the use of Laguerre-Gaussian beams to measure Doppler shifts, and the second exploited interference fringes and corresponding phase reconstruction for detecting reperfusion in microfluidic devices. In its current format, the Doppler system failed to produce results while the phase reconstruction system yielded promising data to illustrate that flow can be detected within different channels. The combination of positive outcomes, through simulation and experimentation, lays the foundation to explore a device that can achieve reperfusion monitoring in a clinical setting.

Keywords

Structured Light, Monte Carlo, Microfluidics, Interferometry, Biophotonics, Homodyne

ACKNOWLEDGEMENTS

I would like to express my sincere gratitude to my supervisor, Dr Akhil Kallepalli, for his instruction, support, and encouragement throughout our work together. I am immensely grateful for all his efforts to allow me to explore fields of research which interest me greatly, as well as for allowing me the opportunity to meet others in the academic community who have helped me grow personally and professionally.

I would also like to thank the members of the Glasgow Optics Group, for their valuable feedback and insights in developing my knowledge and understanding of a new field. In particular, I would like to thank Dr Graham Gibson, Mr Osian Wolley & Prof Miles J. Padgett for their thoughts and contributions to my experimental work. Additionally, I would like to thank Dr Simon Peter Mekhail & Dr Sara Restuccia who helped guide me during the construction of my experimental system.

I would like to extend my thanks to Ms María Cerezo-Sánchez and Dr Finlay Walton with whom I worked closely to develop my theoretical understanding and practical abilities in constructing microfluidic devices. I thankfully acknowledge Prof Hadi Hedari for his supervision and collaboration, without which I would not have been able to explore the field of nanofabrication.

I would also like to thank my Mother and Father, for their continued love and support throughout my entire academic career and beyond. I am eternally grateful for the opportunities for which they have provided throughout my life to explore my love of science.

Finally, I would like to acknowledge the financial support provided by the British Association of Oral and Maxillofacial Surgeons (2021, Research Fund, Endowments Sub Committee), EPSRC Impact Acceleration Account (IAA) [EP/X5257161/1], EPSRC funding to QuantIC [EP/M01326X/1]. All of which have contributed greatly to my professional development.

LIST OF PUBLICATIONS

Accepted

Graham M. Gibson; Robert Archibald, **Mark Main**, Akhil Kallepalli – Modular light sources for microscopy and beyond (ModLight). In *HardwareX Vol. 13, e00385 (2023)*;
doi: 10.1002/10.1016/j.ohx.2022.e00385

Under Review

Mark Main, Akhil Kallepalli – Towards point-of-care diagnostics and monitoring of hypertensive episodes (A Monte Carlo approach). In *Optica Biophotonics Congress: Optics in Life Sciences Conference (2023)*

In Progress

Mark Main, María Cerezo-Sánchez, Osian Wolley, Finlay Walton, Graham M. Gibson, Hadi Heidari, Miles J Padgett, Akhil Kallepalli; – Reperfusion monitoring strategies in visible and infrared wavelengths combining microfluidics and homodyne measurements.

TABLE OF CONTENTS

LIST OF FIGURES

LIST OF TABLES

CHAPTER 1

INTRODUCTION

MEDICAL applications of light have become an increasingly common and promising field of research with exciting new developments in technology. This informs a greater understanding of how light can be used for safe diagnosis and treatment (combined, theranostics is a word now commonly seen in literature). These developments allow more advanced, accurate and/or lower-cost solutions to clinical problems. With cheaper and more sensitive equipment now becoming increasingly available, the use of optical wavelengths of light to carry out imaging, diagnostics and treatment has become a viable modality for use in hospitals and clinics. Overcoming the challenges associated with optical wavelengths to provide accessible and safe diagnostics tools can give people a greater chance of having potential health issues identified at a much earlier stage. It is well known that early identification of most conditions gives patients a much greater chance of making a rapid recovery and a higher quality of life, post-treatment.

Due to the comparatively minimal penetration depth of optical wavelengths of light, *in vivo* imaging can be challenging. Therefore, identifying changes to anatomical structures close to the body surface is ideal for these wavelengths. One such area, subject to substantial changes due to various conditions, is the vascular structure and blood flow. There are numerous conditions that affect how blood vessels function, their structure and their size.

In pursuit of identifying ways to detect these changes, different methodologies must be trialled to find if this is possible using optical wavelengths and if so, which methods prove most useful. By exploring different avenues, both theoretical and experimental, the foundation can be laid for future developments in this field. The work itself and its theoretical underpinning are shown graphically in figure 1.1

1.1 Motivation & Problem Statement

The goal of this study was to explore diagnostic strategies for tissue monitoring and blood reperfusion using optical and infrared wavelengths of light. Motivated by improving the current strategies of qualitative monitoring after procedures such as skin transplants, this research explored orbital angular momentum and homodyne imaging approaches to detecting reperfusion, simulated by flow in microfluidic devices. The long-term goal is the development and introduction of a clinical device that can be used by medical staff to identify whether transplanted skin tissue is receiving adequate blood supply during the healing process, and establish an early detection protocol. This would ensure a positive outcome for patients while minimising the resources spent on resulting repetitive corrective procedures.

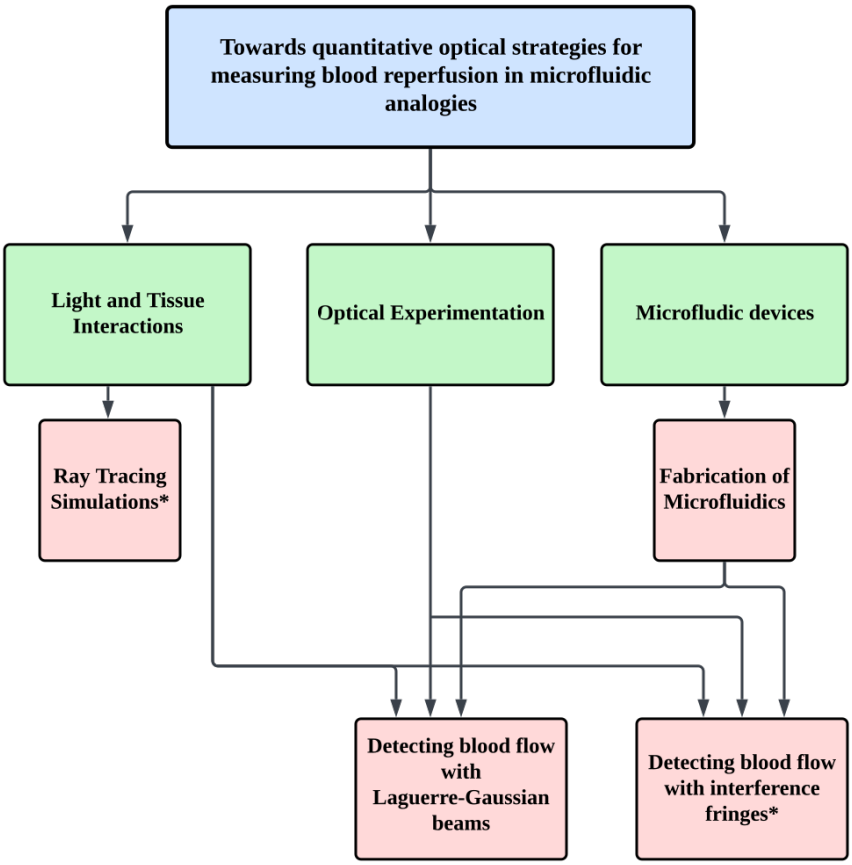

Figure 1.1: *Flowchart outlining the full process of this study, from problem statement (Blue), to theoretical background (Green), and finally the simulation and experimental work undertaken (Red). Each (*) represents a publication generated from the work.*

The ability to image inside the human body has repeatedly shown its benefits since the invention of X-ray techniques. By conducting imaging *in vivo*, medical professionals can ascertain information pertaining to the health and well-being of a patient without any invasive procedures. This enables an informed diagnosis. By identifying issues early, the treatment process has the best chance of success and results in better outcomes for the patient. Although immensely useful, techniques such as MRI and X-rays have limitations and drawbacks of being generally expensive and/or low resolution for tasks such as post-surgical imaging of vascular structures in tissue. Herein lies the value of our methods and outcomes.

The primary objective of any medical procedure is a positive outcome for the patient. In oral and maxillofacial surgery, current procedures of monitoring tissue reperfusion are susceptible to errors, increasing the chances of graft failure. Without access to devices that can quantitatively assess the status of healing vascular structures, patients will continue to endure unnecessary suffering as a result of post-operative issues going undetected by clinical staff. By working towards providing a device which can aid in the monitoring of the patient's condition, a solution can eventually be provided that will improve both the care and outcomes for numerous patients.

1.2 Summary of Main Achievements

The research term was characterised by numerous achievements, altogether serving as milestones while unravelling applications of light transport through tissue.

1. The human wrist model shown in section 3.1, was assessed in a simulation environment to better understand photon interaction with complex tissue structures. An AutoCAD model was designed, and appropriate optical properties were assigned in a ray tracing package (TracePro) for assessment. The simulations have shown that variations in blood vessel geometry produce a substantial variation in scattering within human tissue, forming the perfect platform for future investigations. This simulation assessment is under consideration for presentation at the Optica Biophotonics Congress: Optics in Life Sciences Conference 2023.

2. Through this project term, microfluidic devices were designed and constructed to geometries analogous to human blood vessels. A chrome master mask was designed and externally produced, to be used to make many microfluidic devices, with a range of complexities and sizes to facilitate further work in flow metrics, blood clotting and other biological complications. The construction of the device itself and its use in two experimental systems (sections 3.3 and 3.3.2) showed its application for analysing liquid perfusion within its channels. Manufacturing devices with a range of channel sizes also proved useful in modifying existing SU-8 protocols to better suit finer detailing. This has resulted in the ability to produce many devices with channel sizes varying as much as two orders of magnitude on a single substrate.

The experiments can be broadly separated into two approaches: the first uses an external cavity Helium-Neon laser for generating Laguerre-Gaussian (LG) beams to interact with the fabricated microfluidics, and the second monitors flow in the microfluidic device using a homodyne measurement setup.

3. To generate the LG beam, an external cavity laser was aligned with an intra-cavity wire to produce multiple high-quality Hermite-Gaussian (HG) laser modes. By using cylindrical lenses, Laguerre-Gaussian beams could be produced, which by using additional focusing lenses, could be projected onto a target with variable dimensions. A backscatter collection rig was designed and constructed which can hold six 11 mm Thorlabs fibre collimators at different distances and angles from the target. Although this system did not yield positive results, assessing backscatter can fundamentally be done with the experimental set up in the future.

4. Finally, the flow in the microfluidic device was assessed in a digital holographic microscope system at short wave infrared (SWIR) to determine if phase changes could be identified within the device as blood moves in and out of the vessels. Promising results show the

capability of the system to detect reperfusion in the microfluidic channels, providing a proof-of-concept assessment for applications such as transcranial haemodynamics monitoring; an application that benefits from the NIR window at 1550 nm. This work, combining the microfluidic device and experimental novelties, is being prepared for submission to the journal Biomedical Optics Express.

1.3 Thesis Structure

The introductory chapter gives background information on the interaction of light with tissue, within the scope of biophotonics. Chapter 2 provides an analysis of relevant literature within the fields of research, and frames this work within the wider scope of its domain. Chapter 3 details the methodology that was undertaken throughout the study and provides justifications for the use of these methods (within the scope of the research question). Chapter 4 provides the results of the study and the analysis of the information gathered. Chapter 4 continues to discuss the results of the study and how they are relevant to the domain and the research questions. Finally, chapter 5 provides conclusions to the work carried out, and chapter 6 presents possible improvements and suggestions for future work.

CHAPTER 2

LITERATURE REVIEW

THE background to understanding imaging of the body using light and its relevance in the clinical and consumer domain is inter- and multi-disciplinary. In this chapter, the broad concepts applied in the research study are briefly discussed. These include the basis of light propagation and how it interacts with tissue. The wave and particle aspects of light are used in conjunction to provide meaningful insight into the use of light in identifying changes to material geometries and properties. Experimentally, three concepts are discussed: microfluidic devices and fabrication, generation and application of Laguerre-Gaussian beams and homodyne measurement of flow detection in microfluidic devices.

2.1 Light and Tissue Interactions

The behaviour of light and its interaction with the world around us has been studied for millennia, with new definitions evolving as our understanding improved. Throughout history, light has often been described as propagating in the form of rectilinear rays, as postulated by Euclid's *Optics*, written in 300 BCE. This definition of light would hold as satisfactory until *Opticks*, published by Isaac Newton in 1704 posited that light could be described not as a single ray but as a stream of particles. This theory of particulate light would be disregarded to an extent for another few centuries, as more significant discoveries were made such as those made through Thomas Young's double-slit experiment, where interfering rays of light would only be explained by light propagating as a wave and not as a particle.

It is only in the last century that the current understanding of light was proposed with the theoretical predictions laid down that govern much of modern optics and optoelectronics. In an effort to explain black-body radiation, Max Plank postulates light with frequency v can be defined in quantifiable energy levels.

$$E = hv \tag{2.1}$$

With the constant h to be later named the Planck constant, a critical component in the quantum understanding of light. This equation would suggest that Newton's interpretation of light as a stream of distinct quanta is correct. However, this does not fully satisfy our observations of how light interacts with objects resulting in phenomena such as diffraction. To explain how these particles can behave in light waves, Louis de Broglie proposed that light and its wavelength could be defined in terms of Planck's constant and momentum.

$$\lambda = \frac{h}{p} \tag{2.2}$$

From this, a general theory of wave mechanics was proposed by Erwin Schrödinger, who defined the wave equation in terms of the kinetic and potential energies of a particle. This equation in its general form determines how a system evolves over time.

$$i\hbar \frac{d}{dt} |\Psi(t)\rangle = \hat{H} |\Psi(t)\rangle \tag{2.3}$$

We can make practical use of light by considering it a particle or a wave. In this thesis, light is treated as distinct quanta when considering its interaction with tissue structures within the human body. However, the wave-like properties are manipulated when forming beams with orbital angular momentum (OAM) or exploiting phase and intensity variations between two beams to create images. Understanding the different properties of light and how they can be manipulated is therefore critical for this study.

When considering the interaction between light and human tissue, the variables can be broken down into several fundamental properties. These interactions are defined by absorption μ_a, scattering μ_s, scattering function $p(\theta, \psi)$, anisotropy g, real refractive index n' and reduced scattering μ_s' [1]. These properties govern how light interacts with chromophores within tissue and are useful in simulations. Figure 2.1 shows light interaction as it progresses through skin layers and demonstrates the properties of absorption and scattering.

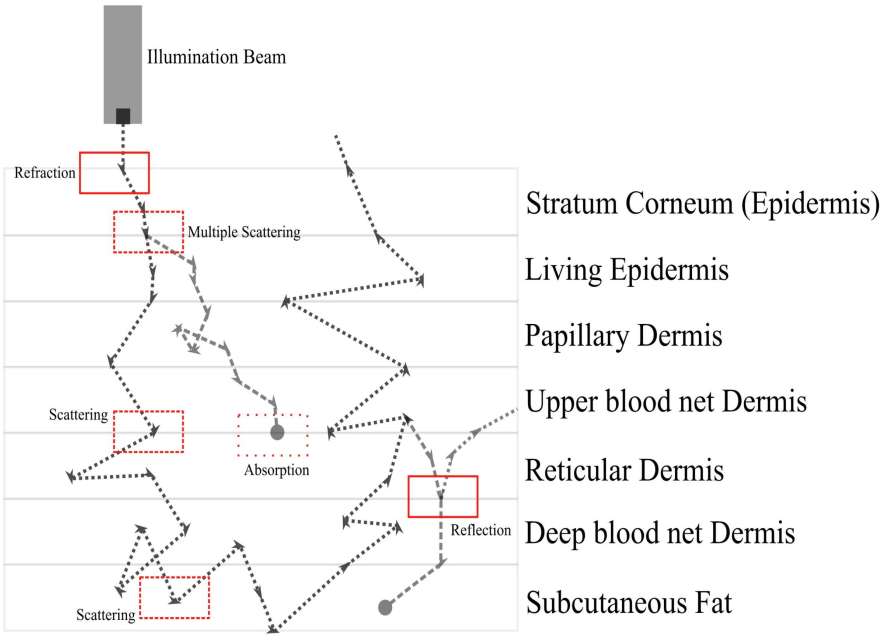

Figure 2.1: *Illustration of the interaction of light within seven skin layers as it undergoes various optical phenomena [2].*

Absorption coefficient relates the total absorbance of a material to its thickness $A = log_{10}[\mu_a]$. This allows the quantification of material absorption as a function of the distance light travels. Scattering itself can be divided into two forms; Rayleigh and Mie scattering. The fundamental difference is considered to be that Rayleigh scattering is linear and is applicable in cases where the particles are smaller than the wavelength of light. Mie scattering applies when the size of the interacting particle is comparable or larger. This, however, is not technically accurate as Rayleigh scattering only refers to Mie scattering below the Rayleigh limit (sub-wavelength particle size) [1]. It is important to note that in the case of multiple scattering events, the nature of scattering becomes isotropic [3]. The scattering, reduced scattering and anisotropy are all related terms with reduced scattering defined in equation 2.4. Anisotropy, defined in equation 2.5, is the cosine of the expected scattering angle when a photon interacts with scattering particles. Each material has an anisotropy value which modifies its overall scattering.

$$\mu_s^{'} = \mu_s(1-g) \tag{2.4}$$

$$g = cos\theta \tag{2.5}$$

Real refractive index (n') is one component of the total refractive index (n), and describes how energy is stored in a medium and its effect on the speed of light. The other component, the imaginary refractive index, describes the dissipation of energy and is another method of determining the absorption coefficient. The total refractive index is given in equation 2.6.

$$n = n' + jn'' \tag{2.6}$$

These properties are required inputs when conducting Monte Carlo simulations for assessing light transport. The interactions within simulations are approximated using scattering functions, which model single-photon interactions. The modified Henyey-Greenstein phase function [4] is the typically used scattering function when simulating biological tissue and is shown in equation 2.7.

$$pHG_{-m}(\mu) = \left(\frac{1}{2\pi}\right)\frac{1}{2}\left[\beta + (1-\beta)\frac{1-g^2}{(1+g^2-2g\mu)^{3/2}}\right] \tag{2.7}$$

This equation produces a probability of a photon scattering at a given angle based on its initial direction. This is modified from the original Henyey-Greenstein phase function to account for multiple scattering events, which is useful in dense media, such as biological tissue. The Monte Carlo simulation software, TracePro used in this study makes use of this phase function.

These optical properties have been quantified for different types of tissues at a wide variety of optical and near-infrared wavelengths of light, allowing the assessment of results and conducting of

simulations to be made simpler as shown in section 3.1.2. This allows simulations to be conducted on multi-layer models with relative ease.

2.2 Optical Experimentation

Manipulation of the wave properties of light through experimentation enables a range of practical applications. From optical modulation where certain properties of light are used for tasks such as information transfer, to interferometry where the interaction of multiple waves can be used to gather information about the wave source.

Light has both linear and angular momentum with the angular component consisting of both spin (associated with polarisation) [5] and orbital components (associated with spatial distribution) [6]. Non-degenerate laser modes can be produced which contain well-defined orbital angular momentum known as Laguerre-Gaussian (LG) modes, by transforming them from Hermite-Gaussian (HG) modes [7]. The LG laser modes propagate as a helically phased beam with different modes resulting in varying phase and intensity patterns on the image plane. The generation of these waves can be achieved through numerous different methods. The simplest method uses a set of cylindrical lenses to convert HG modes to LG modes [8]. Other methods include the use of a fork diffraction grating, which can also be achieved using spatial light modulators (SLM), i.e. liquid crystal on silicon (LCoS), digital micromirror devices (DMD) [9], metamaterials [10] and multi-plane light conversion (MPLC) (which can be used to multiplex modes) [11]. These approaches span a wide range of costs and complexity, each with their own advantages and disadvantages [12].

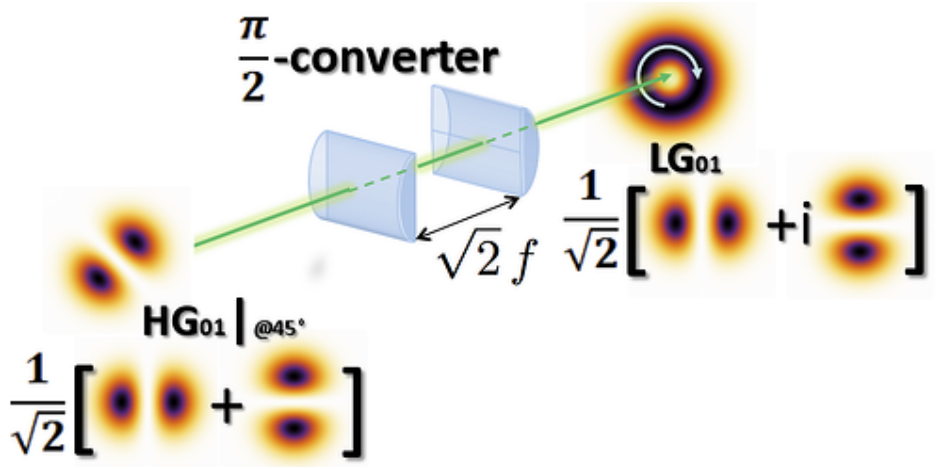

Figure 2.2: *Illustration of the conversion from a HG_{01} beam to an LG_{01} beam [13].*

In this study, cylindrical lenses are used to generate LG modes from HG modes. The conversion from HG to LG laser modes using a set of cylindrical lenses is the most mathematically accurate method of producing low-loss LG beams, due to its direct manipulation of the Gouy phase [7]. The conversion itself requires two cylindrical lenses to be placed in the beam path with a distance between them of $\sqrt{2}$ of the focal length of the beam. By tilting the lenses to a 45° angle normal

to the incoming HG beam, a phase transformation is carried out on the beam producing a helically phased LG beam. The limitation of the cylindrical lens is that it is prone to alignment issues and can only produce the LG beam at the output that corresponds to the HG beam at the input. Figure 2.2 shows the implementation of a cylindrical lens for converting HG to LG beams.

LG laser modes have seen application in a variety of fields, most noticeably in optical tweezers [14] where the vortex at the centre of the beam is able to hold objects in place and manipulate them. It was identified that these laser modes could be used in the field of free space communications [15] from which, high-speed communication methodologies were developed utilising the properties of OAM [16]. This allowed the development of communication systems with free space [17] and fibre [18] transfer speeds in the Tbits/s scale. The detection of orbital angular momentum in single photons [19], has been utilised in quantum mechanics for cryptography [20] and shows violations of Bell inequalities [21]. In biology, LG beams and the manipulation of orbital angular momentum have found some success with microscopy techniques, such as spiral phase contrast [22] and enhanced edge detection [23].

The properties of light can also be exploited through the interference of multiple beams. Interferometry is the practice of interfering two waves to produce a new wave with an amplitude composed of the difference in the amplitudes of the two input waves. The most famous use of this technique is the Laser Interferometer Gravitational-wave Observatory (LIGO) which was able to detect ripples in space-time (gravitational waves) resulting from the merger of two black holes [24]. The principles of interferometry have also seen use in microscopy, first devised in 1950 [25]. One of these techniques, Digital Holographic Microscopy (DHM), takes a single beam and splits it into two components, a signal and a reference beam. By sending the signal beam through a sample, recombining the beams and imaging the resulting beam on a camera, a reconstruction of a digital hologram can be formed for both phase and intensity [26].

2.3 Microfluidics

Microfluidic devices have seen substantial uptake in research and commercial use. Most notably in lateral flow tests (a form of paper based microfluidic first introduced in 2007 [27]) which saw a surge in popularity during the COVID-19 pandemic. These devices are developed in a wide variety of materials and have a large number of uses in many sectors from drug discovery to point of care diagnostics [28]. Due to the relative infancy of this technology, many new devices are being manufactured using microfluidics as novel approaches to long-standing problems. By utilising factors like small channel formations to study blood cell deformation for personalised medicine [29], or flexible materials being used to create sensors and improve processes like mixing and pumping [30].

Microfluidic devices have seen applications in liquid transport as they can be designed to meet a number of size and flow rate requirements needed to simulate human vascular structures [31] (this

study is the primary reference for the fabrication of devices for optical experiments). They can be manufactured to sizes smaller than 10 μm allowing channels as small as capillaries to be made. Creating different conditions using these fluidic channels allows various parts of vascular anatomy to be replicated and tested accurately, helping to test both the ideal light sources and sensors as well as allowing the basis of the signal processing algorithm to be written with known conditions such as flow rate and vessel size.

Additive and subtractive methods can be used in nanofabrication to remove or add material to the substrate and create channels. Subtractive processes involve the removal of a material, generally using etching [32], whereas additive processes build material on top of a substrate using multiple techniques such as spin coating and sputtering [33]. For creating hollow channels to mimic veins and arteries, an additive process is best as it allows a 'master' mould to be made, followed by the addition of the base material to hold the channels themselves, in this case, polydimethylsiloxane (PDMS). This method is simple and cost-effective as many devices can be made with relative ease from a single master mould, provided adhesion between the photoresist and the substrate is sufficient. Figure 2.3 shows a simplified method used to create a PDMS-based microfluidic device.

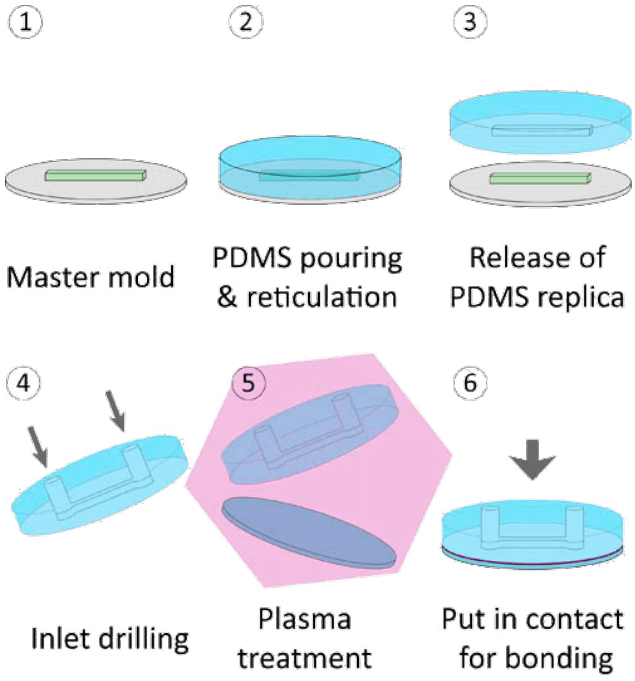

Figure 2.3: *Additive process used to produce PDMS-based microfluidic device [34].*

PDMS is a material commonly used in microfluidic devices and has been deployed in a wide variety of devices with many applications [35]. It is cheap, easy to manufacture, bio-compatible and has low optical absorption at a wide range of wavelengths (shown in figure 2.4) making it easy to observe the behaviour of liquids passing through the channel. These factors make PDMS an ideal material for use in proof of concept studies due to its versatility and few drawbacks.

Microfluidics provide the ability to perform experimental work on precisely manufactured chan-

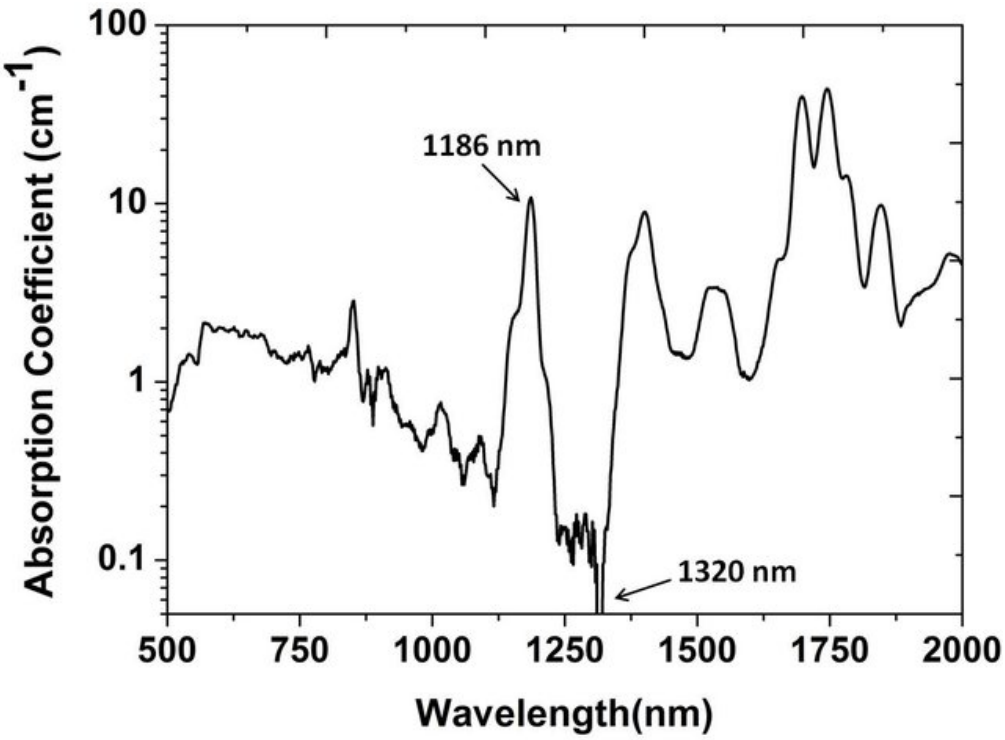

Figure 2.4: *Graph of optical absorption of PDMS from 500-2000nm [36].*

nels akin to those found in the body. Unlike using real tissue, microfluidics are easier to work with, require no extensive ethical approval process, and the optical properties are better understood than the complex structures found in human skin. They have found uses in biophotonics, in their own field of optofluidics, for many applications such as on-chip flow cytometers [37] and microbiological sample analysis [38]. This makes microfluidics ideal for a range of optical experiments due to their versatility. It is thanks to this versatility that microfluidic devices are an ideal choice for use in a range of optical experiments.

2.4 Evolution of optical wavelengths in biological measurements

The field of non-invasive medical imaging is one of the most useful tools available for diagnostics in the clinical and consumer fields with a wealth of techniques commonly used [39]. The field has seen rapid growth and change in recent years, particularly in devices that can take simple measurements at a low cost such as wearable smart devices [40]. The capabilities of these devices and their accuracy has improved substantially. Modern devices are able to perform functions such as pulse oximetry, tracking sleep data based on heart rate and even assisting in performing electrocardiography without the need for numerous electrodes, as seen in traditional devices [41]. The ever-reducing costs of sensors and light sources, as well as the increased processing capacity of these devices, has facilitated the development of new metrics to be measured. These developments in combination with an increased consumer and clinical interest in health metrics have allowed for a substantial uptake in small-scale measurement and processing measurements, with predicted

compound annual growth rates of 28.1% until 2030 [42]. As a result, there is a push to expand the capabilities of these small-scale devices to measure health metrics in greater detail and develop methods of assisting the diagnosis of a greater number of health conditions. Increasingly in the consumer market, these devices and studies that make use of large datasets obtained from them, aim to measure/analyse metrics that can be used as a marker for developing health conditions [43] [44] [45]. In this context, the use of such devices is to help identify conditions at the early stages or predict the likelihood they may arise using data trends.

Light has many practical uses in the medical field, including its incorporation into diagnostic procedures and surgical techniques [46]. One of the most famous imaging techniques utilised in hospitals, Optical Coherence Tomography (OCT) [47] is able to produce high-resolution *in vivo* images in the optical and infrared regimes. It has found numerous uses such as endoscopy of the gastro-intestinal tract [48], retinal imaging [49] and identification of plaques as a sign of heart disease [50]. The ability to operate with non-ionising radiation and produce high-quality images at a cellular level on living tissue within the body makes this an incredibly useful tool. Infrared light can be utilised further in functional near-infrared spectroscopy (fNIRS), to detect changes in haemoglobin concentration. This allows the diagnosis of mental health disorders and the study of neurological development, motor control and perception, and cognitive function [51]. Another major field which incorporates optical wavelengths is theranostics. The combination of therapeutics and diagnostics - theranostics, whether in the context of imaging or treatment, leverages the optical response of certain chemicals to light in order to aid in diagnostics, drug delivery and treatment response monitoring [52].

CHAPTER 3

METHODOLOGY

THE methodology of this study covers four broad tasks completed during the research term: ray tracing simulations, microfluidic device fabrication and two optical experimental strategies. This is outlined in figure 3.1.

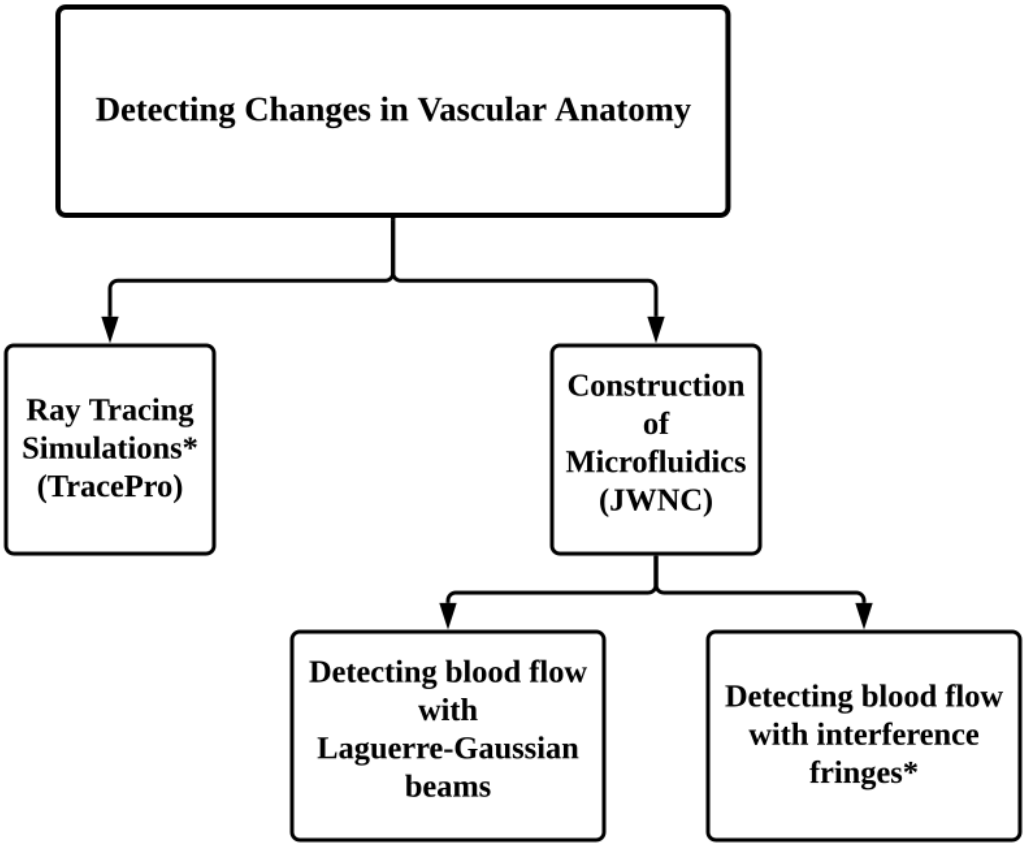

Figure 3.1: *The flowchart outlines the workflow of the studies including simulations, microfluidic device fabrication and optical experiments. Each (*) represents a publication that has been produced as a result of the work carried out.*

A novel complex geometry model of the wrist/forearm was designed in AutoCAD for assessing photon propagation through ray tracing simulations. Subsequently, optical properties were assigned to each material within the model and the photon interaction at a wavelength of 633 nm (Red) was quantitatively assessed.

Experimental work includes microfluidic device fabrication and optical experiments. To produce a proof-of-concept assessment for a strategy to monitor reperfusion, we assess optical interaction in microfluidic devices. This begins with adopting a fabrication strategy and modifying it for

this specific application. Building on Fenech *at al.*'s work [31], a modified fabrication technique was developed to generate channels with a minimum width of 7 μm to mimic vasculature in tissue, without standard fabrication techniques.

The optical experiments include two quantitative approaches: (1) to generate LG laser beams and assess how they are transferred to be vertically incident on the microfluidic device. (2) to assess flow in the context of reperfusion into transplanted tissue, utilising a homodyne measurement technique.

3.1 Ray Tracing Simulations

To conduct pilot studies, particularly in areas that require ethical approval for experimental work such as biophotonics, Monte Carlo software is a useful tool for optical simulations as it allows initial testing of hypotheses without the need for a clinical study. Monte Carlo simulations in their simplest form are random number generators that are used to find the probability of a certain outcome from a system. These simulations see wide use in numerous sectors from business risk analysis to the video games industry. Ray tracing has become an increasingly popular area of research, especially in real-time applications due to the extreme computational demands these simulations produce. In the context of optical modelling, Monte Carlo is useful for simulating light interaction in complex systems, as optical properties identified from experimental literature can be assigned to materials while up to trillions of virtual photons can be introduced into the system. One such software package that allows this kind of complex optical modelling is TracePro. This package permits the import of AutoCAD models to be used as the geometry through which light transport can be modelled. This facility grants the user the ability to create intricate models and assign structures different optical properties.

3.1.1 Geometric Model

To conduct optical simulations of how light behaves in the human body with anatomical variations, a model of a wrist/forearm was produced in AutoCAD. By segmenting this model into different 'layers' these sections can be extracted separately and recombined in ray tracing software to define the optical properties of each tissue type within the model. Due to the penetration depth of the light source concerned being limited to a few millimetres [53], the ligaments, tendons and muscle fibres can be simplified into a single 'base material'. In this study, the primary focus is to identify changes that can be detected in and around the skin-level structures based on geometric changes to vessel structures within the tissue.

Skin tissue itself is a highly complex structure with numerous layers each performing a different function. For this model, a two-layer skin model was chosen, consisting of the epidermis (surface) and dermis (subsurface). The epidermis is a thin layer of cells that serve to protect the body from light, abrasions and harmful organisms [54]. Due to the lack of blood, the optical properties of

the epidermis are purely dictated by the concentration of melanosomes (melanin) [1]. Surface blood vessels are contained within the dermis and serve to provide oxygen and nutrients to the skin. The dermis can be subdivided into a number of layers, the deep net, the reticular layer, the upper blood net and the papillary dermis. For these simulations, the dermis will be combined into a single layer. This is due to both a lack of absorption and scattering data available, as well as the computational demands created by such a complex CAD model. The vessel structure has been simplified from those found in real tissue, with all vessels smaller than the main veins and arteries made into cylinders which span the entire model. This reduces the complexity of the geometry thereby reducing the overall computational load. The model also does not contain other common tissue inclusions such as hair follicles, nerves and sweat glands. This is due to the complexity of these structures and the difficulty of implementing them, both geometrically and identification of appropriate optical properties.

The model was produced by first measuring 100 mm of the forearm to gain approximate outer dimensions which were used to build an outer framework. The two major bones present in the forearm, the radius and ulna, were added from where the forearm meets the wrist to 100 mm up the forearm. A curved grid/mesh was then produced which encircled this area, modelling the curvature of the outer wrist. This provides attachment points for splines to be produced that follow the geometry of the wrist, thereby producing the paths the veins and arteries will follow. Circles were made with the outer diameters of these vessels and then extruded along the paths created, modelling the non-linear paths that veins and arteries can be seen to follow. The venules and arterioles, however, are much smaller and have a much denser distribution. As such, it would be impractical to replicate the previous method of manually creating each vessel. To produce these vessels, cylinders were created to represent the vessel walls and the blood within and extended to the full length of the model. At this point, an array function was used to replicate these vessels numerous times. By doing this with the arterioles and venules, a model with over 1000 elements can be produced. To finalise the model, the base muscle layer, the subcutaneous fat, the dermis and the epidermis must be added to the model, separate from the vessels they contain. To do this, the vessels are copied and the layer is extruded over the original vessel structure, subsequently followed by a subtraction. This leaves the base material with hollow areas where the vessels were positioned. At this point the copied vessels are moved to the original position giving two distinct parts that can be separated with no overlap. This is repeated for the dermis layer and finally, the epidermis is added onto the exterior, with no requirement for subtraction as it contains no vessels. Figure 3.2 shows a cross-section of the CAD model with each type of tissue generated in different layers with varying colours to better visualise the geometry.

In order to better visualise the light interactions within the tissue and how the light reaching parts of the tissue is changed by vessel size, numerous detectors were added within the dermis and muscle. All the detectors were given dimensions of 0.5 mm^3 with the intention of assigning

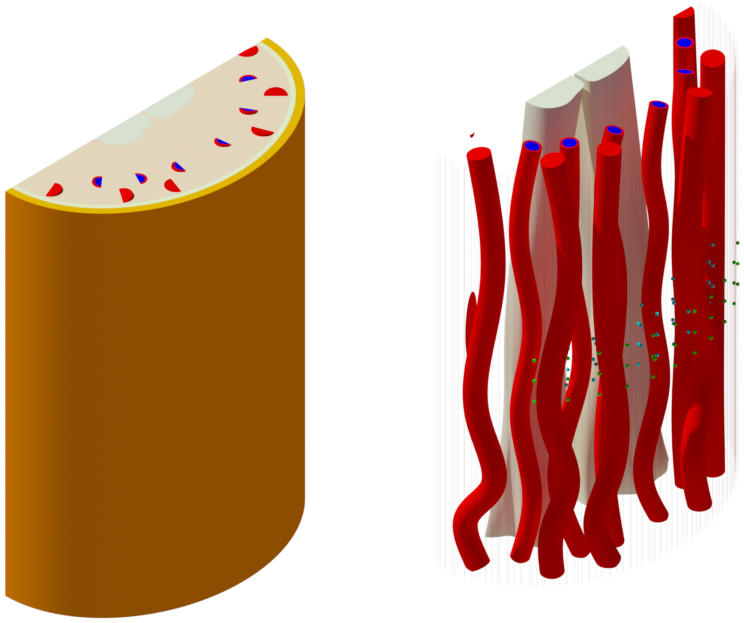

Figure 3.2: *CAD model of the human forearm with and without skin and muscle layers. The image on the right highlights the geometry of the larger blood vessels.*

optical properties equal to that of the tissue they were contained within. This allows the ray paths to continue as they would if no detectors were present. The dermal detectors were placed within close proximity to the arterioles and venules, and the muscle detectors were placed before and nearby the arteries and veins to quantify an increase in scattering caused by the changes in vessel walls. All the detectors can be seen with an X-ray view of the forearm in figure 3.3.

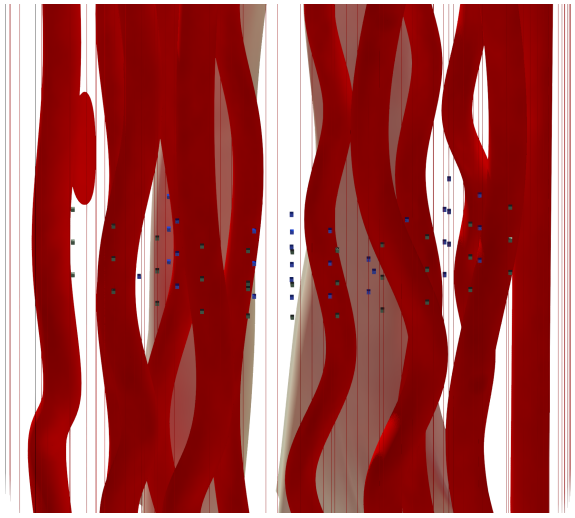

Figure 3.3: *Detectors within the forearm model. Green detectors are those within the dermis and blue are those within the muscle.*

To distinguish a healthy tissue model from an unhealthy tissue model, the vessel wall size of both the larger and smaller vessels were doubled, as shown in figure 3.4. This increase in wall thickness corresponds to the effect caused by conditions such as hypertension. This could be due to a build-up of fatty deposits or hypertrophy of the muscle tissue as a result of a consistent increase in blood pressure. In the case of this model, the increase in thickness is due to thicker vessel walls and modelled as double the thickness (in comparison with the healthy model).

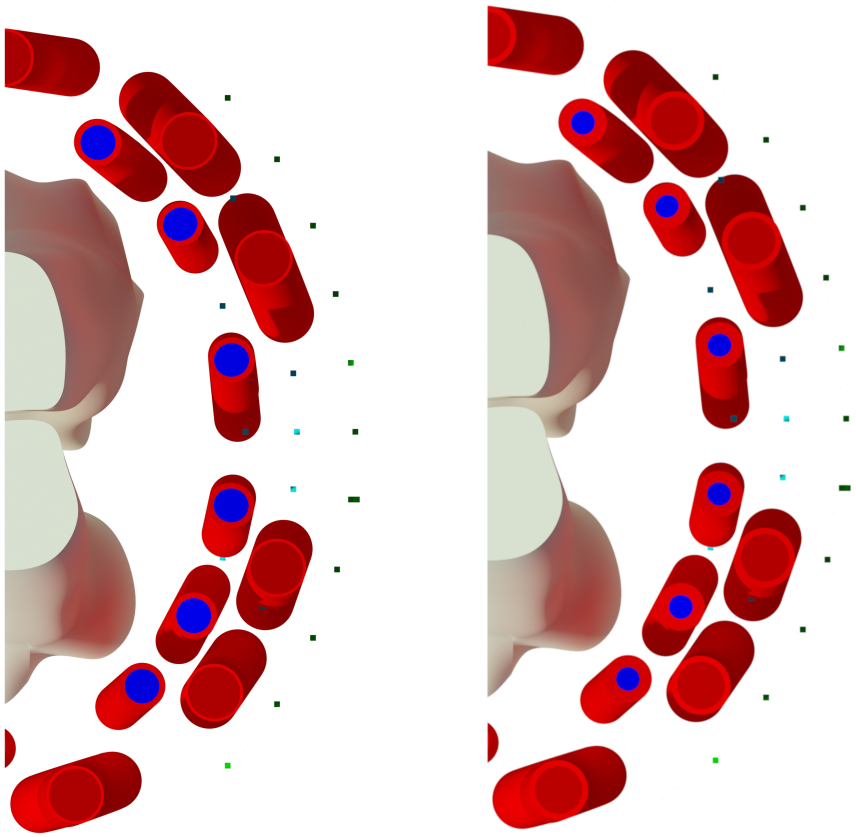

Figure 3.4: *Top view of cross sections in both healthy (Left) and unhealthy (Right) models.*

These models are copied into the simulation environment and each assigned the same optical properties for each layer. This allows the detection of variation solely based on variations in the geometries of the models.

3.1.2 Optical Properties

All simulations in this study are carried out at 633 nm with optical properties of each component and total flux set to simulate a Helium-Neon (HeNe) laser used in the LG beam experimental set-up in section 3.3.

Due to the many tissue types used in this model, an extensive search of experimental literature is required to identify the properties needed. The four key properties required for simulations on TracePro are absorption coefficient, scattering coefficient, anisotropy factor and refractive index. Optical absorption measurements are widely available in literature due to their relative ease of experimental measurement in most tissue types. Some tissue layers such as the epidermis, dermis and fat have numerous components which contribute to their absorption coefficients. The absorption coefficient of the epidermis is calculated using equation 3.1.

$$\mu_{a.epidermis} = (\mu_{a.melanin})(f_{melanin}) + (1 - f_{melanin})(\mu_{a.skin}) \tag{3.1}$$

Equation 3.1, is a simplified version that ignores the individual layers found in the epidermis and focuses on melanin, the primary chromophore. Epidermal absorption is quantified using base melanin absorption ($\mu_{a.skin}$), and a volume fraction ($f_{melanin}$) which varies with each individual. By varying the volume fraction of melanin, in accordance with the Fitzpatrick skin type scale [55], simulations can be conducted focusing on six skin types ranging from Type I (palest) to Type VI (darkest). For these simulations, an average value was taken of Type III and IV as this represents the mid-point of the human population and gives substantial absorption and scattering of incident light on the tissue. The volume fractions for each skin type of the Fitzpatrick scale are shown in table 3.1.

Table 3.1: *Volume fraction values for Fitzpatrick skin types [55]. These values were averaged in sets of 2 to give a broader spectrum. 0.134, shown in bold is the average value used in the simulations.*

Melanin Volume Fraction for Fitzpatrick Skin Types					
Type I	Type II	Type III	Type IV	Type V	Type VI
0.029	0.045	0.126	0.142	0.263	0.346
0.034		**0.134**		0.304	

To calculate the absorption in the dermis, a number of approximations are required due to the heterogeneity of the tissue itself and the variety of chromophores found within.

$$\begin{aligned}\mu_a^{dermis}(\lambda) = (1-S)\,\gamma\,C_{blood}\,\mu_a^{Hb}(\lambda) + S\,\gamma\,C_{blood}\mu_a^{HbO_2}(\lambda) + \\ (1-\gamma\,C_{blood})\,C_{H_2O}\,\mu_a^{H_2O}(\lambda) + \\ (1-\gamma\,C_{blood})(1-C_{H_2O})\,\mu_a^{(0)}(\lambda)\end{aligned} \tag{3.2}$$

Equation 3.2 calculates the absorption coefficient of the dermis [1]. The parameters used are

the primary absorbers of blood, concentration (C_{blood}), deoxygenated haemoglobin ($\mu_a^{HbO_2}(\lambda)$), and oxygenated haemoglobin ($\mu_a^{Hb}(\lambda)$). Typical values of oxygen saturation (S) and hematocrit (γ) were also taken into consideration. By finding these values for a given wavelength, the absorption of the dermis *in vivo* can be estimated with relative accuracy. This equation was used for calculating both the absorption of the dermal layer and the subcutaneous fat layer, as equation 3.2 produces dependable values for the fat found in the skin layers.

Scattering in tissue is substantially more challenging to calculate and is generally identified on a case-by-case basis, without generalised equations. Scattering or reduced scattering in this study was identified in the literature. In the case of reduced scattering, anisotropy values are used to find the scattering. Generally, reduced scattering is found using equation 2.4, however, by rearranging this equation, scattering can be found from reduced scattering if the anisotropy is known (which is based on the cosine of the expected scattering angle, Eq. 2.5).

Table 3.2 shows the optical properties assigned to each tissue layers and their dimensions. Table 3.3 shows optical and geometric properties of all vessel walls and the blood within. Appendix A.1 provides a full table of optical properties for three skin types and the values used to calculate the epidermal, dermal and fat properties.

Table 3.2: *Optical properties of tissue layers for skin type 3/4 on the Fitzpatrick scale used in simulations. Values have been taken from literature to define optical and geometric properties [56–63] Values in bold have been calculated based on other values in the table found in the literature.*

Layer	Epidermis	Dermis	Fat	Homogeneous Muscle	Bone
$\mu_a(mm^{-1})$	5.09	0.03	0.02	0.12	0.06
$\mu_s(mm^{-1})$	**29.67**	**26.82**	5	**10.45**	33.47
g	0.82	0.9	0.75	0.9	0.9
η	1.34	1.4	1.44	1.38	1.56
$d(\mu m)$	0.1	1.83	1.14	56-70 mm	-

Table 3.3: *Optical properties of vascular structures used in simulations. All vascular walls have been assigned the same properties due to the absence of reliable literature on each type. These values were found from a range of sources [64–71]. Values in bold have been calculated based on other values in the table found in the literature.*

Layer	Arteriole (wall)	Arteriole (blood)	Venule (wall)	Venule (blood)	Artery (wall)	Artery (blood)	Vein (wall)	Vein (blood)
$\mu_a(mm^{-1})$	0.12	0.29	0.12	2.61	0.12	0.29	0.12	2.61
$\mu_s(mm^{-1})$	**16.19**	356.87	**16.19**	335.76	**16.19**	365.87	**16.19**	335.76
g	0.87	0.99	0.87	0.99	0.87	0.99	0.87	0.99
η	1.33	1.37	1.33	1.37	1.33	1.37	1.33	1.37
$d(\mu m)$	20	10	2	18	1000	3000	500	4500

3.1.3 Simulation Environment

To compare the difference between healthy and unhealthy models and their interaction with light, two simulations were conducted with identical parameters. By using TracePro, each of the layers designed in AutoCAD which correspond to each material type is defined separately.

Once a model is imported, the layers can be named corresponding to their material and the properties can be set. Each material is assigned an optical absorption (mm^{-1}), scattering (mm^{-1}), anisotropy and refractive index. The wavelength of light is defined, in this case, 633 nm, as the software itself can support multiple wavelengths in a single simulation. The numerous detectors within both the dermis and the muscle could cause an issue with the optical path of the rays. To resolve this, the detectors were assigned to two objects, dermal detectors and muscle detectors. Once assigned, the dermal detectors were given the optical properties of the dermis and the same was done for the muscle detectors. This allows the path of the ray to remain uninterrupted, but still allows the square surface of the detectors to be inspected and compared across simulations. A hollow sphere is added around the wrist model and is set to be a perfect absorber. This serves dual purposes; to reduce the computational demands of ray tracing far outside of the relevant geometry and more importantly, to visualise any changes that occur in reflection between the two simulations as the long-term goal following this study is to measure light with a device after it has left a system.

To conduct the simulation, a source must be created which has the properties of a desired beam that would be sent into a practical system. Unfortunately, the implementation of structured light, such as beams with orbital angular momentum is impossible and so in this case a Gaussian beam is used. A circular beam was generated with a radius of 2.5 mm with coordinates (75,75,50) from the origin set at the base of the forearm model. The normal vector of the beam is then set to (-1,-1,0) allowing the beam to the aimed at a 45° angle to the origin. The resulting beam is 30 mm from the exterior of the model which is typical of what might be found in a handheld non-contact device. Some of the beam parameters must then be set. The total flux of the beam is set to 5 mW which corresponds to the midpoint between a class 3R and 3B laser which is safe for short-term skin exposure. The spatial and angular profile of the beam is then set with the axis deviation and beam divergence of a CPS635 collimated laser diode module (Thorlabs, Inc.), as this is a widely available laser diode that may be used in a finalised device. Lastly, the wavelength is set to 633 nm corresponding to a HeNe laser.

The model itself, with a circle denoting the beam source, is shown in figure 3.5 before the simulation is conducted on the healthy model. The sphere around the model has been made transparent in this case to allow inspection of the model.

The software allows two simulation types, analysis mode and simulation mode. Analysis mode stores the traced ray paths in the Random Access Memory (RAM) and displays a desired number of traced rays and their entire path within the model. Simulation mode requires the assignment of exit surfaces, with the light interactions with these surfaces to be stored in non-volatile storage.

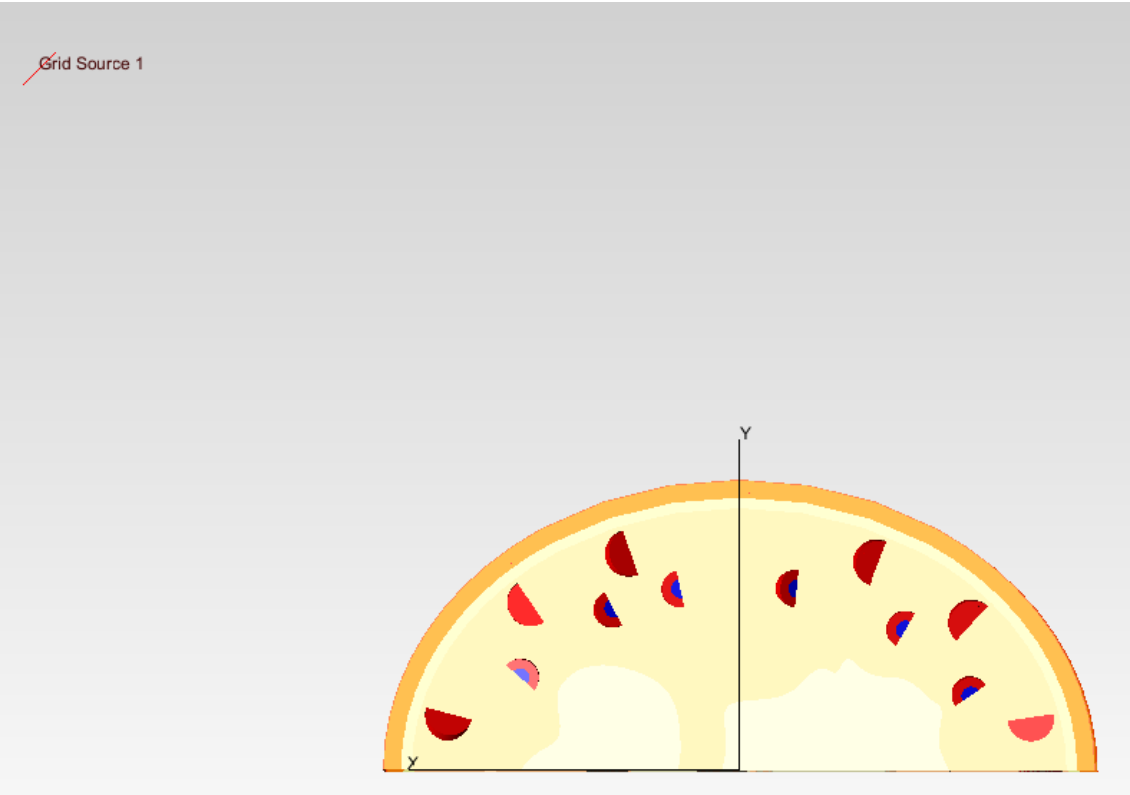

Figure 3.5: *Pre-simulation image of forearm model within the TracePro simulation environment. Grid Source 1 denotes the origin point of the incident beam.*

Generally, simulation mode is better for millions to trillions of photons while analysis mode can be used if the system RAM is sufficient. In this study simulating 1,000,000 photons approximately corresponded to a requirement of 50 Gb of RAM. Analysis mode was used in these simulations as it allows the visual inspection of a set number of rays within the system, and the hardware on which TracePro was run holds a large amount of memory. Both simulations were conducted with 850 rings, resulting in a simulation of 2,164,951 photons incident on the model. The result of these simulations are shown in section 4.1.

3.2 Experimental Proof of Concept

To test any optical experimental strategy, a system analogous to the problem statement is needed. This is achieved by fabricating microfluidic devices that geometrically mimic the blood vessels in the tissue. Subsequently, the devices are used in two experiments: measuring the backscatter of LG beams incident on a device, and a digital holographic microscope system to detect fluid flow (in transmission).

3.2.1 Microfluidics

The microfluidic devices fabricated in this study are designed to mimic the types of structures found in human skin tissue. Unlike typical microfluidic designs, which feature only a few chan-

nels, designs for this system must be non-linear and have diverging channels of varying sizes. The implementation of these features presents challenges at each stage due to difficulties in manufacturing. Despite this, the process to create these devices still follows a standard design procedure highlighted in figure 3.6.

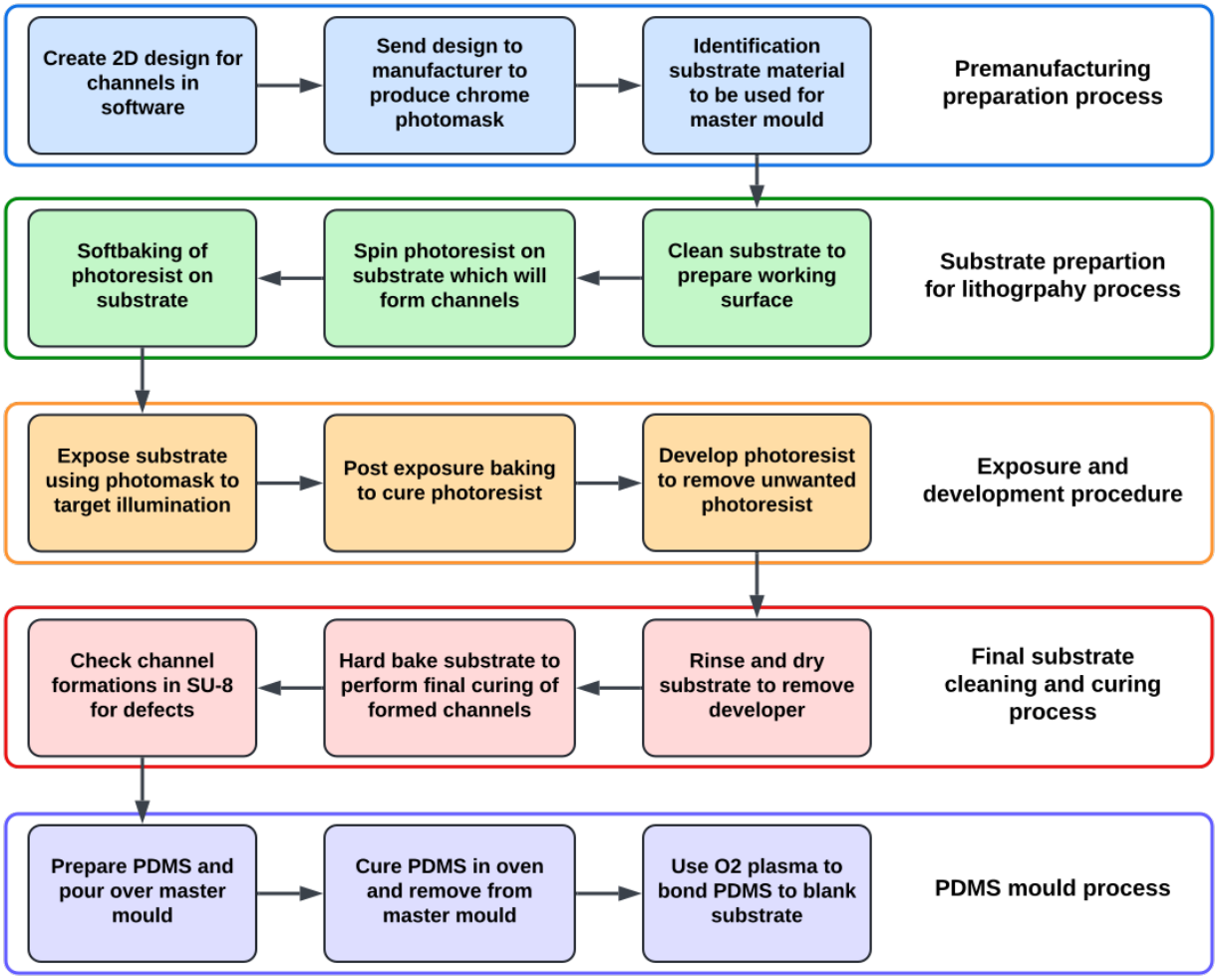

Figure 3.6: *Flowchart outlining standard microfluidic mould design and manufacturing process.*

Device Design

To implement a microfluidic device that is analogous to a vascular structure, a custom chrome master photomask which contains a number of templates that accurately reflect the vascularity of the body was designed. Some designs were provided by authors of Fenech *et al.* [31]. As well as these designs, simpler designs were produced with some modifications made to size and structure. Numerous designs at a variety of sizes were developed as a built-in redundancy measure since the manufacturing process is complex and error-prone at the intended scale. The inclusion of many designs also maximises the 4“x4” (100 x 100 mm) area provided by the photomask to facilitate future research beyond the scope of this work.

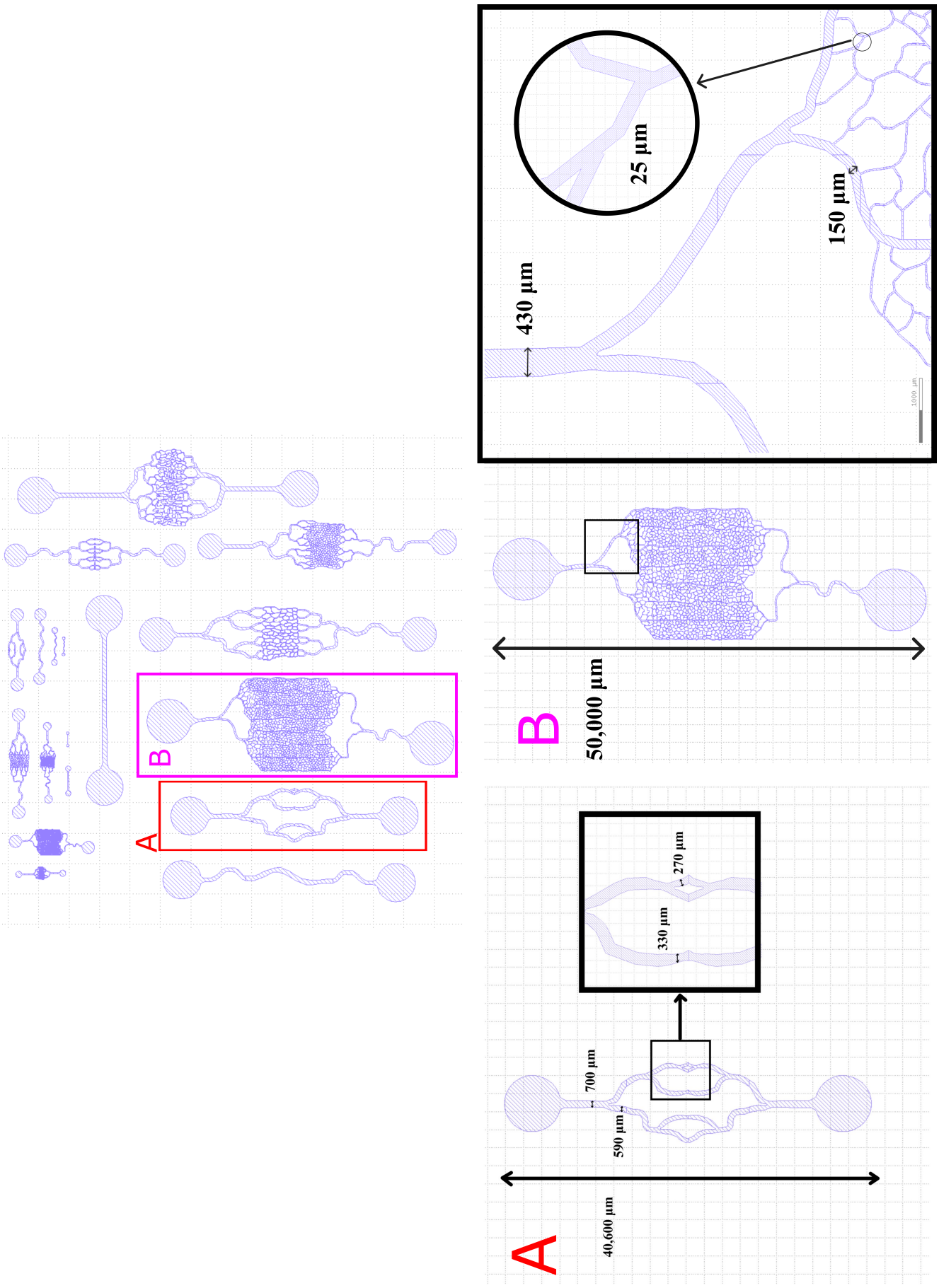

Figure 3.7: *Full design sent to a external manufacturer. Individual devices A and B show a sample of channel sizes within the design.*

Figure 3.7 shows the design produced in software to be sent to an external manufacturer. The features themselves range in width from 500 μm to 5 μm which corresponds to the widths of the range of blood vessels found within human skin. Figure 3.7 also shows sections of two of the complex designs with labelled channel widths. The gradual reduction of vessel sizes corresponds to that seen in skin vasculature as the structure branches off into smaller branches until they reach capillaries. The mask itself was designed on KLayout and this design was sent to Compugraphics for external manufacturing. The 4"x4" chrome mask is formed from a quartz substrate with a layer of chrome deposited on one of its surfaces which has sections removed to replicate the design provided.

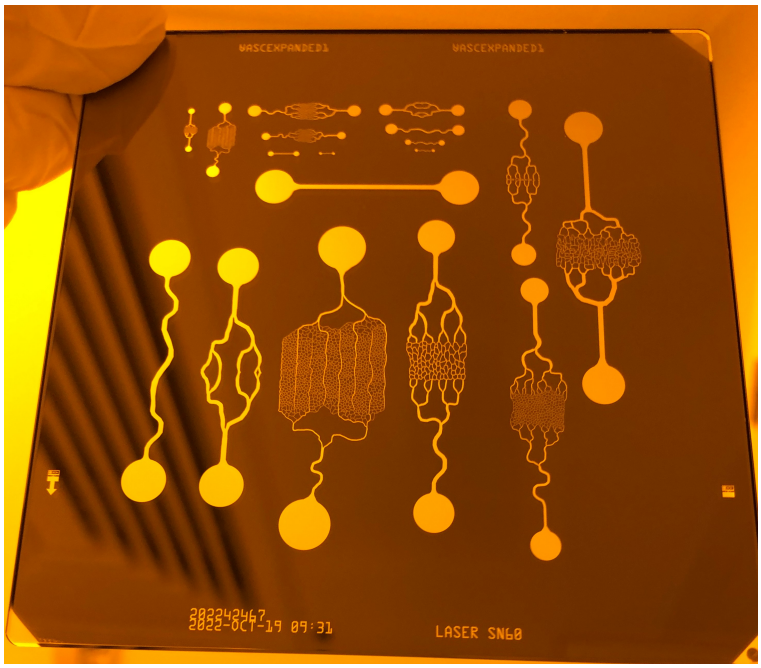

Figure 3.8: *Chrome master used in photolithography exposure procedure.*

Figure 3.8 shows the photomask manufactured by Compugraphics to be used in the photolithography process. The photomask in this case is a negative mask as the photoresist used (SU-8) hardens when exposed to UV light. Therefore, the transparent regions match those of the desired patterns to create the master pattern for the microfluidic device.

The mask is stored in a clean room environment as any dirt or dust on the surface can occlude light during the exposure process. Due to the complexity of the structure and the variations in feature size, the initial attempt uses a standard SU-8 photolithogrpahy and development procedure [72]. It was predicted that the variations in feature sizes would cause issues with the standard process. Through retrospective analysis of the final device, insight could be obtained as to possible improvements should the first version give a poor outcome or fail completely. A glass substrate was chosen for this attempt due to its low cost, given the likelihood more attempts would be required.

Substrate Preparation

To prepare the glass substrate, a standard solvent-cleaning process was used. The substrate is placed in a beaker of Opticlear and rests in an ultrasonic bath for five minutes. The substrate is removed from the beaker and rinsed with acetone before being placed in a beaker full of acetone. The beaker is then placed back in the ultrasonic bath for an additional five minutes. This rinse and replace procedure is then repeated with methanol followed by rinsing with reverse osmosis (RO) water. Once rinsed, a nitrogen (N2) gun is used to dry the substrate, as well as preventing water staining.

The cleaned substrate is primed for the application of a photoresist. An appropriately sized vacuum chuck is attached to a spinner, which holds the substrate firmly in place during the spinning process. The spinner is then programmed to dissipate the photoresist to the desired thickness. The program is set to spin at 500 rpm for 5-10 seconds with an acceleration of 100 rpm/second, and then spun at 1000 rpm for 30 seconds with an acceleration of 300 rpm/second. The spinner is tested to confirm desired operation and accurate alignment of the substrate. Upon completion of these checks, SU-8 3050 photoresist is dispensed onto the substrate until it is half covered as shown in figure 3.9. At this stage, it is crucial to remove any bubbles found within the photoresist. The presence of bubbles following spinning can cause damage to the channels during the development process. Next, the spinner is activated and the programmed procedure is completed. The vacuum is turned off and the substrate is removed. The bottom edges of the substrate are wiped using a cotton swab with acetone to prevent any unwanted SU-8 from sticking to its holding case in between procedures.

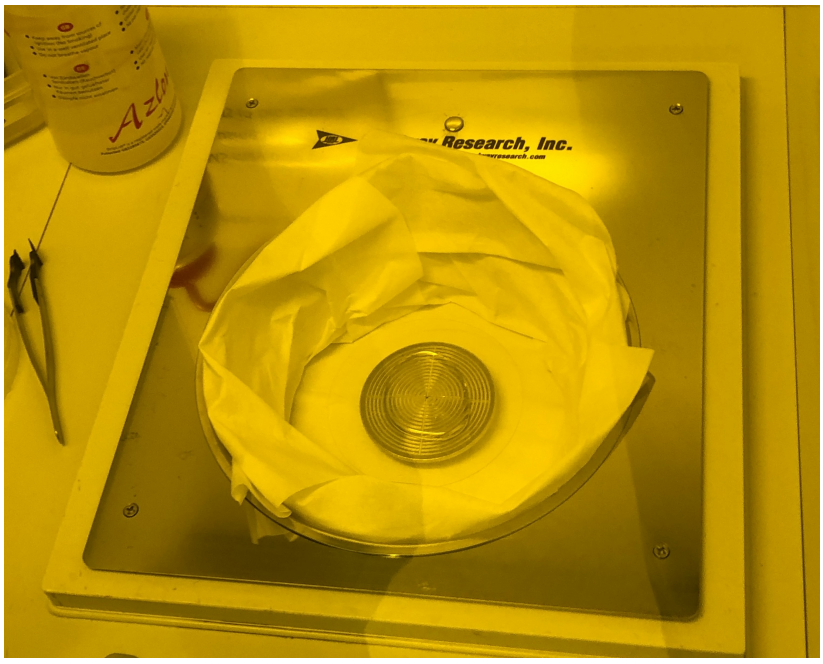

Figure 3.9: *Spinner with SU-8 3050 deposited on working surface prior to spinning.*

Following the spinning process, the substrate is immediately placed in an oven to soft bake at $95°C$ for 45 minutes. This partially hardens the SU-8 before photolithography which improves the quality of the exposure process by evaporating the solvent within the SU-8 and hardening it.

Exposure and Development

After the soft baking, the substrate can undergo the photolithography process. The substrate and photomask are placed in the appropriate positions within a SUSS MA6 photolithography machine shown in figure 3.10. The gap between the mask and substrate is set to 50 μm with exposure time set to 20 seconds at an energy level of $18.4 mJ/cm^2 s$. The calculation used to find the exposure time is shown in appendix B.2 and is derived from the datasheet for SU-8 3000 [72]. The device is activated and the substrate is exposed to UV light through the photomask, illuminating sections in the pattern of the desired channels. The UV light causes the SU-8 resist to crystallise, forming a stronger lattice which can prevent developers from removing it. Due to the proximity of the substrate to the photomask, some of the SU-8 stuck to the bottom of the photomask and had to be removed with acetone.

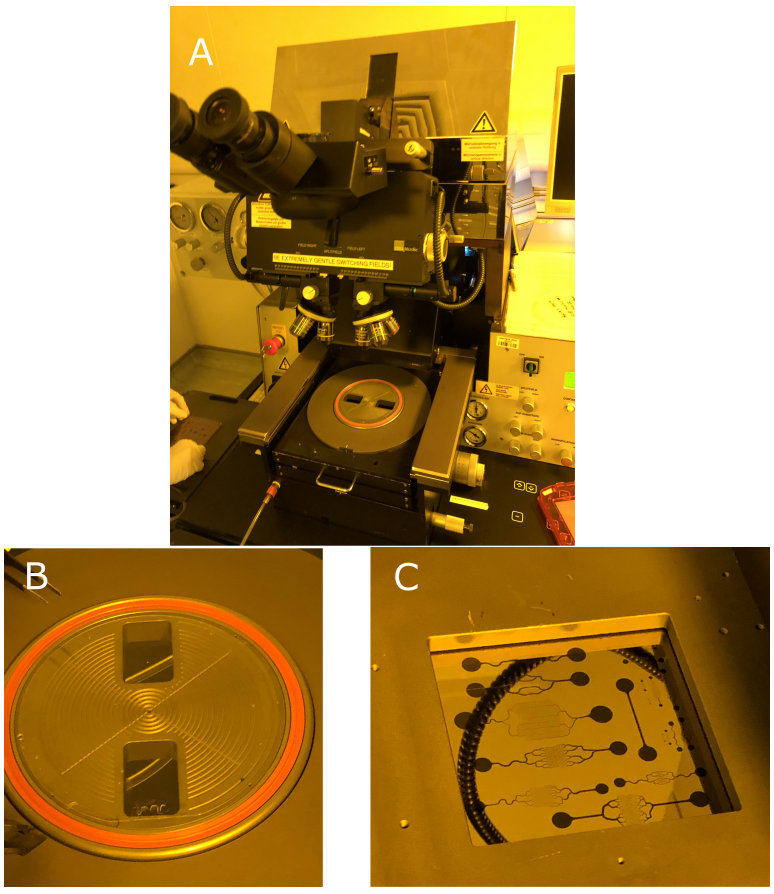

Figure 3.10: *Exposure stage for microfluidic devices. (A) shows the MA6 photo-lithography machine prior to the placement of the block holding the chrome master. (B) shows the glass substrate resting on a vacuum check used to hold it in place when inverted. (C) shows the chrome master held within the MA6.*

After exposure, the substrate must be baked again in order to give the SU-8 the needed energy to undergo the hardening reaction, known as the post-exposure bake. This process requires 1 minute at 65°C, followed by 5 minutes at 95°C.

The development process is challenging due to the channel sizes and the mask. As it is difficult to determine during the process itself whether the developer has removed enough SU-8, the standard time was chosen of 15 minutes for 100 μm thick film channels. Placing the substrate within a beaker of ethyl lactate and strongly agitating the beaker for 15 minutes, the developer removes the uncured photoresist. Once this process is carried out, the substrate is cleaned for 10 seconds with fresh developer followed by a final spray of developer. The substrate can then be dried with an N2 gun to remove any remaining fluid from between the channels.

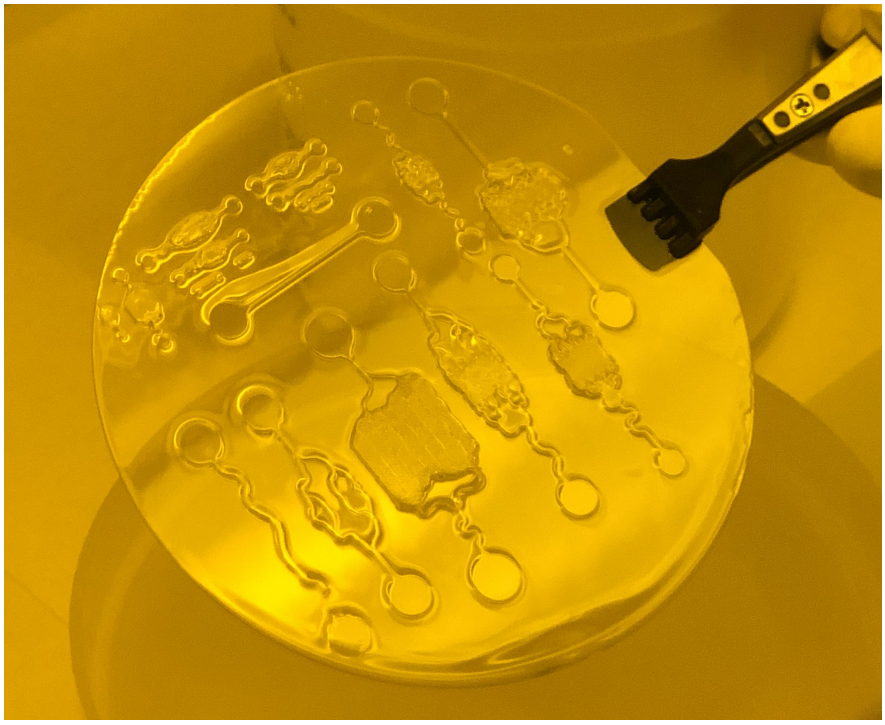

Figure 3.11: *Glass substrate following the development process.*

Shown in figure 3.11 is the glass substrate following the development process before drying with the N2 gun. Upon close inspection, it can be seen that the larger channels are well-defined. However, the smaller channels have not been very well developed and are not sharp. Some of the features on this substrate also appeared to have detached from the glass which could be seen when the pressure of the nitrogen from the N2 gun was acting on the features. In figure 3.12 the channels can be seen under a microscope. Although easily distinguishable, they have poorly defined edges. This issue is mostly likely caused by insufficient development time in an attempt to preserve the smaller channels.

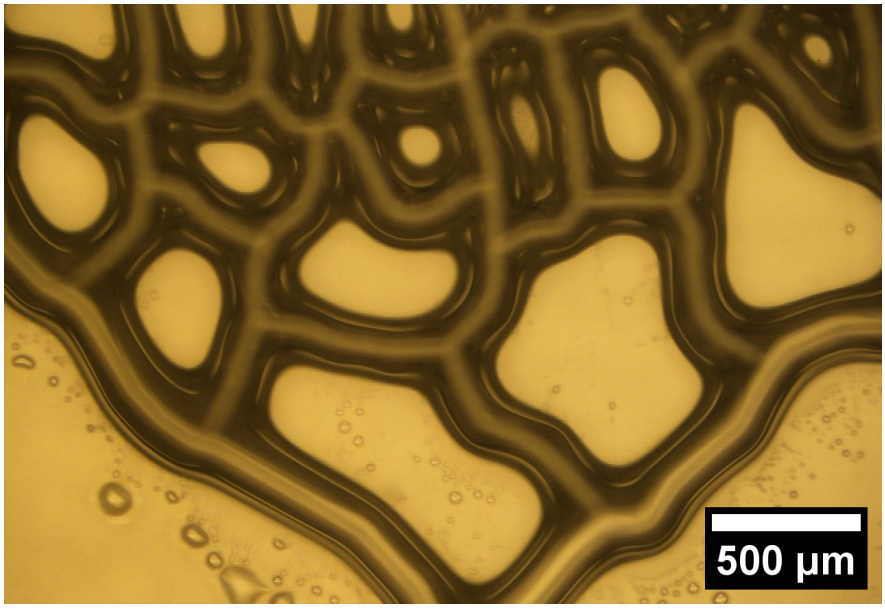

Figure 3.12: *Microscope images of channel outlines on the glass substrate following the development process.*

To finally cure the SU-8, a hard bake is required which includes three steps. These are (1) bake in the $90°C$ oven for 15 minutes, (2) $180°C$ oven for 1 hour and then (3) in the $90°C$ oven again for an additional 10 minutes. During the baking process, some of the detached channels appear to have re-bonded to the glass substrate, although the strength of this bond later transpired to be fairly weak.

PDMS Mould Process

After hard baking, what remains is a glass substrate with a thin layer of hardened SU-8 in the shape of the desired channels on top. This substrate functions as a master mould for the microfluidic device.

Polydimethylsiloxane (PDMS) is a clear polymer used to form the channels of the device as discussed in section 2.3. The liquid form of PDMS is mixed in a 10:1 ratio with an elastomer curing agent until the resulting liquid is full of bubbles. In this case, 20 g of PDMS and 0.2 g of curing agent were used, requiring a mixing time of 7 minutes. The liquid is then placed in a degassifying chamber with a low vacuum created inside to remove the bubbles. The chamber has a small easy-release valve on top to relieve pressure without deactivating the entire system. The mixture bubbles over intermittently which can be stopped with the valve of the chamber being opened for a few seconds. This cycle is repeated until all of the bubbles formed within the mixture from the mixing process are removed. This step is crucial as bubbles within the PDMS can not only cause issues with the resulting channels but will cause issues in imaging systems due to the refractive changes.

When adding the PDMS to the substrate itself, one challenge is that PDMS is a viscous liquid

until cured in the oven, and so has a tendency to flow away from the substrate. To combat this, a small enclosure was designed to be attached to the substrate. Once the enclosure was placed, UV-activated glue was applied to the base of the enclosure and activated. Slow pouring of the liquid until the desired thickness is reached whilst ensuring no new bubbles are introduced during the pouring process. The 20 g quantity yielded a block of PDMS with a thickness of 4 mm across the substrate. Once the liquid is poured, the substrate can be placed inside a hotplate oven at 85°C for 2 hours to fully cure the PDMS. Once the curing is complete, the PDMS and substrate are left to cool for a few minutes before extraction.

Normally, PDMS can then be removed with a scalpel, and to preserve the SU-8 structure for future fluidic devices to be made, a small drop of IPA is placed between the PDMS and substrate to easily detach the two sections. In this case, the PLA enclosure caused some issues and partially bonded with the PDMS during the curing stage. This may be due to PLA being known to be slightly porous and so could have allowed liquid within the structure itself, which then hardened. As a result, removing the PDMS was challenging and resulted in irreparable damage to the master mould, with the glass substrate breaking.

To complete the final device, the PDMS block must be reattached to another blank substrate. Using a scalpel, relevant sections of the PDMS block were removed in order to be bonded to glass slides. Both the PDMS and glass slides were cleaned using the same cleaning process outlined in section 3.2.1. By exposing the PDMS and glass to O2 plasma, the surfaces of the PDMS and glass are left with silanol (SiOH) groups on the surface which makes the surface more hydrophilic. The PDMS and glass can then be placed in contact creating a bond between the surfaces that generates a seal which can not be reversed, thereby leaving only the desired channels for the liquid to travel through. The glass and PDMS were exposed to plasma with a power of 80 W for 20 seconds inside a Plasmafab 505 Barrel Asher. Figure 3.13 shows the asher used to expose the PDMS. Both the glass substrate and PDMS are placed inside the barrel on a glass dish.

The last step is to create holes to form inlet and outlet channels which are produced by using a small tool to press into the PDMS at the desired diameter for the microfluidic tubing needed. This allows the final device to be tested to assess any leakage and confirm the operation of the device. A final device is shown in section 2.3.

Figure 3.13: *Plasmafab 505 Barrel Asher used to expose PDMS and glass substrate.*

Updated Complex Procedure

In order to improve the outcome of the complex procedure from the initial attempt, a number of key changes had to be made. The resist process had to be re-evaluated to obtain higher quality channels that do not detach from the substrate and have sharper, more well-defined edges. This is especially important for smaller features which tend to amalgamate into an undefined globule of photoresist. The substrate must also be made from a stronger material to reduce the chances of shattering allowing multiple PDMS moulds to be made. Finally, the device must have a thicker layer of PDMS to support the syringe tubing in the inlet and outlet channels.

A prediction was made that the best method to improve the quality of the channels would be to perform a longer soft bake. This would cause additional hardening of the SU-8 to a greater extent, reducing the amount of exposed SU-8 being stripped away by the developer.

The full procedure was repeated with a silicon substrate of the same size as the glass substrate with the soft baking time increased to one hour. During the development of the photoresist, it was concluded that the development process had been carried out sufficiently after 13 minutes, as a visual inspection showed sharp channel outlines.

Figure 3.14 shows a number of microscope images taken of the photoresist on the silicon substrate following the development process. The edges of this channel in this iteration have a greater definition than that of the glass substrate shown in figure 3.12. Although slightly rounded channels would be ideal when replicating a blood vessel network, this property could not be achieved in larger channels without sacrificing the structure of the smaller-width channels.

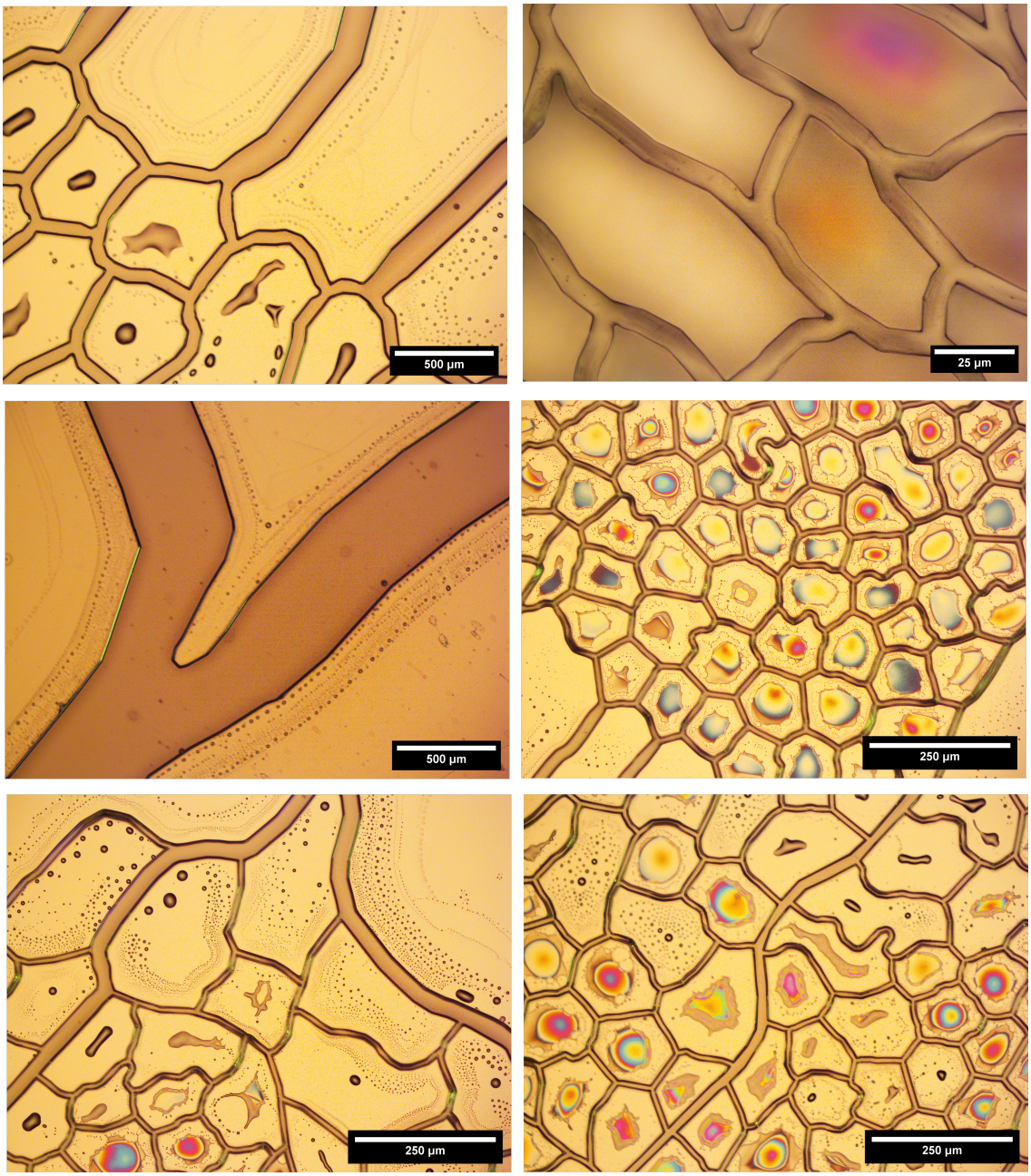

Figure 3.14: *Microscope images of channel moulds created on the silicon substrate.*

Figure 3.15 shows the silicon substrate with channels following the full development process. When compared to the glass substrate, the clarity of channels appears much clearer.

The resulting PDMS mould formed using the silicon substrate had a much greater level of detail than that of the initial test. Figure 3.16 shows the resulting PDMS channels formed which have highly defined sharp channels in sections with large and small widths.

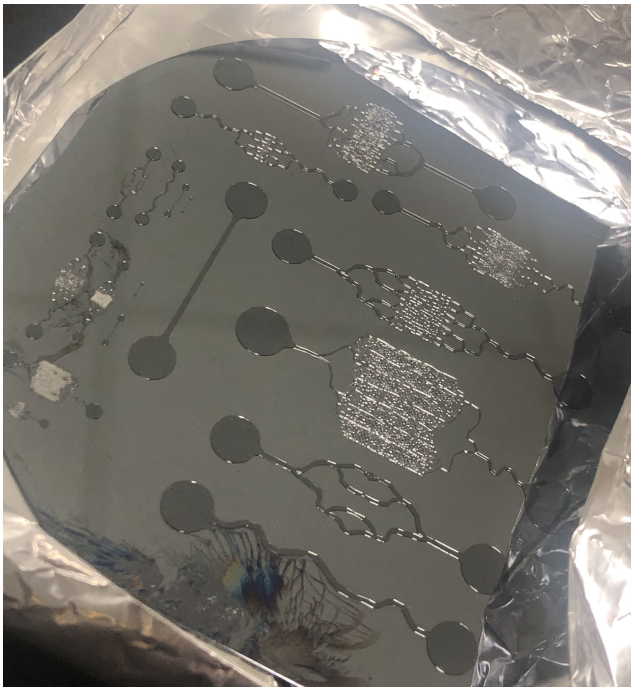

Figure 3.15: *Silicon substrate with raised channels following the SU-8 development process.*

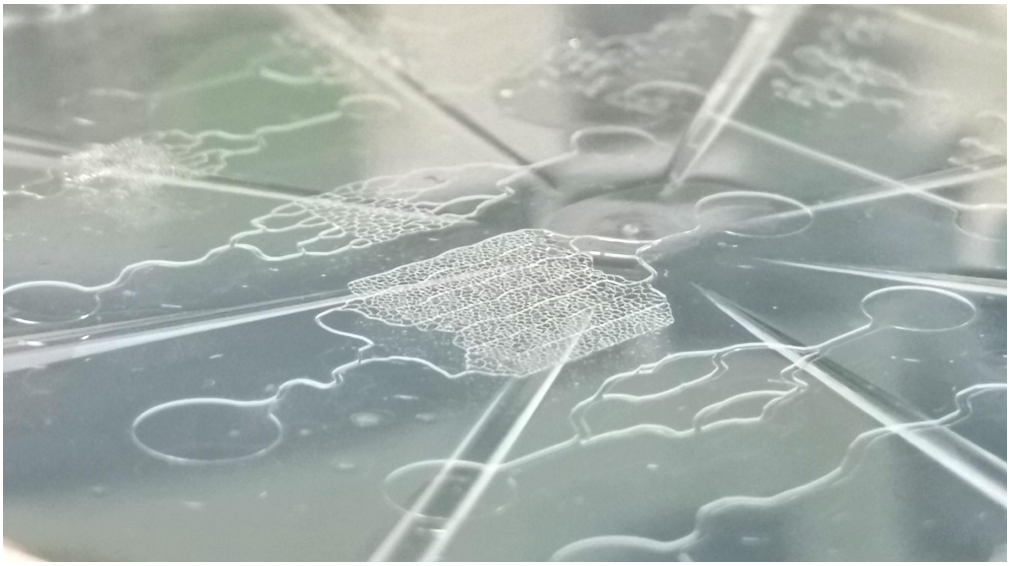

Figure 3.16: *PDMS mould formed following removal from SU-8 master.*

3.3 Optical Experimental Strategies

Two experimental strategies were trialled during this study to measure flow within the microfluidic device. The first system, shown in section 3.3.1, was constructed with the goal of measuring changes using LG beams. The second experimental strategy, shown in section 3.3.2, utilises a previously constructed homodyne microscope.

3.3.1 Laguerre-Gaussian System

To find blood vessel variation and fluid flow, this system uses a Laguerre-Gaussian (LG) beam incident on a microfluidic device with fluid flowing through it to image the movement of liquid through the channels by collecting backscattered light. The set-up can be split into two sections, the beam generating stage which produces the LG beam, and the collection stage which takes backscattered light and amplifies the signal to be interpreted by a LabView program. An external cavity HeNe laser at a power of 5 mW was used to generate a Hermite Gaussian (HG) beam by using a Brewster window and misaligning the planar mirror at the other end of the cavity. The cavity itself was configured at a length of 150 mm which is ideal for the power produced by the laser. Figure 3.17 shows the external cavity laser.

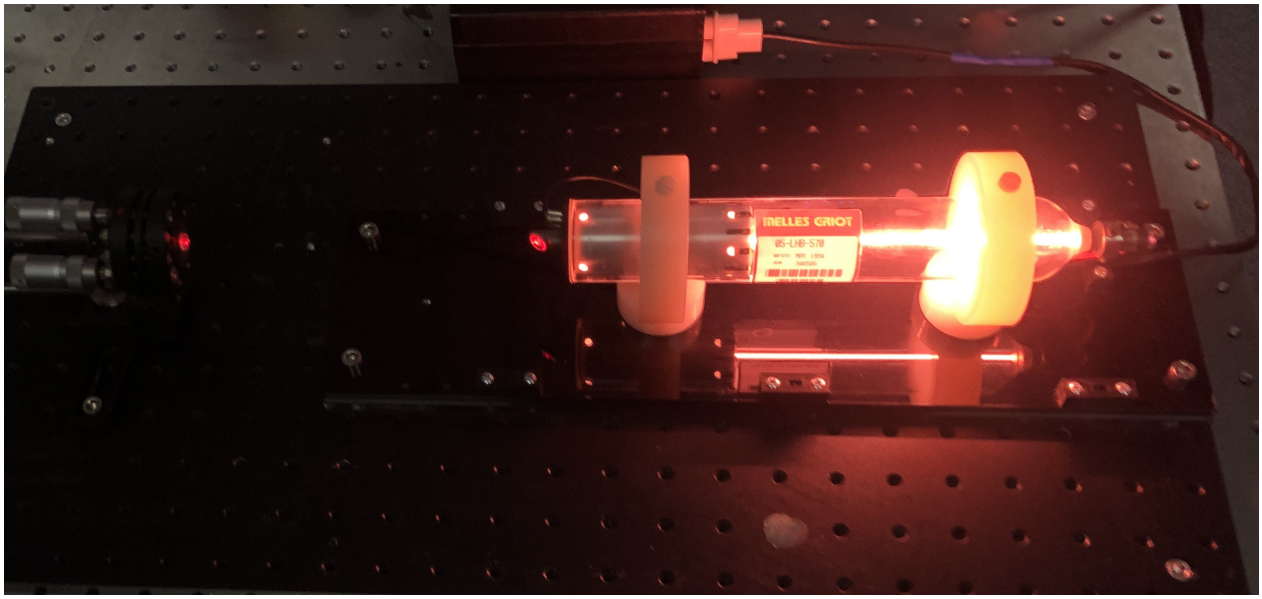

Figure 3.17: *External Cavity Helium-Neon laser. Configured with a 150 mm cavity length at a power of 5 mW.*

A much shorter cavity length was trialled in an attempt to make the system more compact. However, the resulting HG and LG beams were highly elliptical in nature which was likely due to instability in the output laser modes. The cavity itself is challenging to align and requires precise manual alignment to obtain high-quality laser modes at the output without astigmatisms warping the resulting beam on the image plane. To improve the quality of the beam an intra-cavity nanowire was included which is suspended between the output of the Brewster window and the planar mirror, shown in figure 3.18. This is crucial when considering how an intra-cavity inclusion alters the beam as it is introduced. As the inclusion stops light passing a particular point, losses begin to build up within the cavity at that position. By adjusting the position of the wire, there is an alteration in which modes suffer the greatest amount of loss. Lasers will always output the mode which incurs the least amount of loss. The adjustment of the wire within the cavity, as well as the alignment of the planar mirror itself in conjunction with the wire, can produce higher quality modes with less

effort than the mirror alone. This method allows this kind of laser to access higher-order modes, however, for this use case, there is no requirement for high-order laser modes. As a result, a single vertical or horizontal wire interrupting the beam path within the cavity is sufficient. Higher order modes would require a cross wire, one vertical and another horizontal, although this may be better achieved using a spatial light modulator. Commonly used spatial light modulators include liquid crystal on silicon (LCoS) SLM and digital micromirror devices (DMD).

Figure 3.18: *Planar mirror of external cavity Helium-Neon laser with intra-cavity wire to produce high-quality modes.*

The improvement in the output laser modes is substantial however would likely not be required if the laser used was not an external cavity. To test the quality of both the HG and LG beams, a camera is required to image the intensity of the beam components. For this a DCC1545M - USB 2.0 CMOS Camera, 1280 x 1024, Monochrome Sensor (Thorlabs, Inc.) was chosen. This is crucial when finding if null zones in the HG and LG beams do in fact have small amounts of light, which are difficult to see with the human eye. Due to the power of the laser and the sensitivity of the camera, a series of neutral-density (ND) filters were placed after the cylindrical lenses in order to reduce beam intensity. Depending on the numerical aperture of the beam, the ND filters were varied accordingly to allow all parts of the beam to fit within the 0-255 greyscale pixel range allowed by the camera. The nanowire and the tilt of the planar mirror were then adjusted to produce a variety

of HG modes to check for output quality in case higher-order modes were eventually required. Neutral density filters were placed in front of the camera to reduce the amount of incoming light reaching the sensor, preventing saturation of the pixels. Figure 3.19 shows a few HG laser modes captured on a the camera.

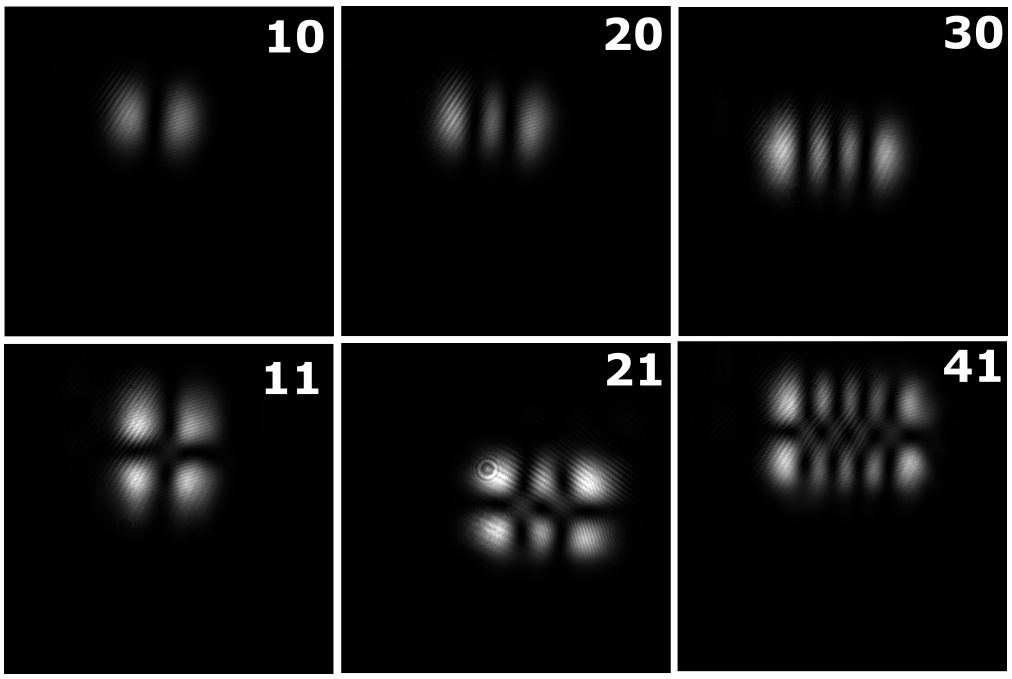

Figure 3.19: *Hermite-Gaussian modes captured on a standard 255-bit scientific camera. Each image is labelled with its mode number.*

Once a desired HG mode is produced, in this case, a 10 mode, the beam must be focused and any astigmatisms produced by the laser or focusing lenses are removed. The HG beam is focused through an f 160 lens with an iris on either side of the lens to remove astigmatisms allowing a high-quality HG beam to be produced. This was verified using a beam profiling program on MATLAB which converts the pixel values taken from the camera image and creates a contour plot [73]. The beam profiles can be seen in section 4.3.

To generate a beam with orbital angular momentum from a Hermite-Gaussian laser mode, a set of cylindrical lenses can be used to change the phase of the beam with minimal losses. There are numerous ways to produce an LG beam, however, they mostly produce impure beams with substantial loss. The cylindrical lenses mathematically and physically implement a theoretically perfect phase transformation on the beam. This is why the HG beam required to create this beam must be of high quality as the transformation is exact and without loss, without a way to compensate for astigmatisms. Any astigmatism, misalignment or incorrect angular orientation of the cylindrical lens will produce an LG beam that is poorly defined or elliptical. These factors make aligning such a system challenging as the absence of adaptive optics necessitates manual alignment of all components and repeated checks to assess if the quality of the beam reaching the image plane is

improving or degrading based on the changes made. Figure 3.20 shows the full system used to generate LG laser modes.

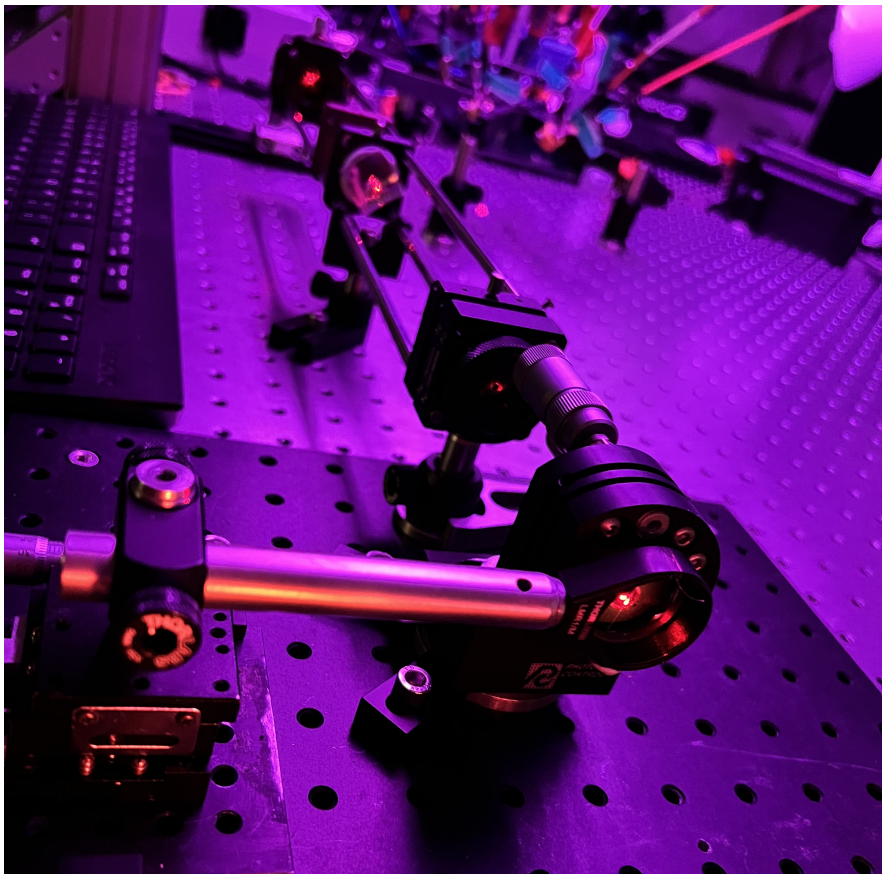

Figure 3.20: *Optical system to produce Hermite-Gaussian beams and transform them into Laguerre-Gaussian beams.*

To determine the quality of both the HG and LG laser modes, a CMOS scientific camera and beam profiling programs were used [73]. The results of this process are detailed in section 4.3.

Once a high-quality low order LG beam is produced, a lens is used to focus the beam allowing the numerical aperture at the incident point on the microfluidic to be easily adjusted to meet the size requirements of the channel it is interrogating. The beam is reflected along a set of three mirrors that transfer it onto a rig allowing the final beam to be vertically incident downward onto the microfluidic device. By doing so the liquid within the device is not subject to a flow difference as a result of gravity when turned on its side. It also allows for radial backscatter collection to be implemented with less difficulty.

Figure 3.21 shows the transmission optics used to transfer the generated LG modes to illuminate the microfluidic device vertically. Once the light encounters the microfluidic and the liquid within the channels, it undergoes scattering which must be collected to interpret for any data.

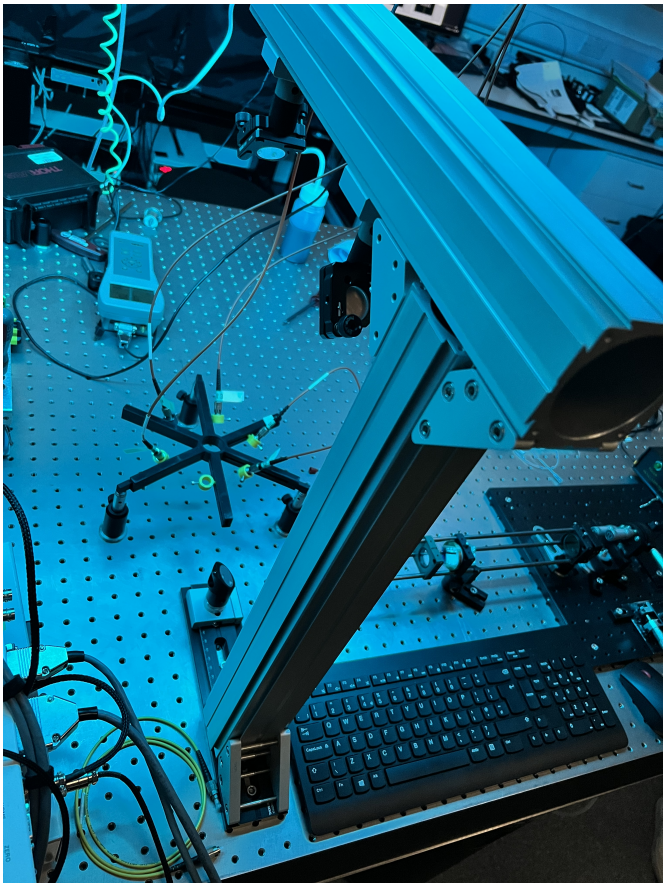

Figure 3.21: *Reflection rig used to take horizontal beam and redirect it upward to allow vertical incidence on the microfluidic device.*

Backscattered Light Collection

The backscatter collection is carried out using a radial array of six fibre collimators focused on the incident point of the LG beam. The rig was designed with two key considerations. Allowing a wide range of positions to be chosen for fibre collimators and having a large central hole to allow the incident beam to pass through the centre of the rig.

The initial design used 3 sets of 2 arms which could rotate using ball bearings. This design, although structurally sound had one key issue. By having layered arms there is some inconsistency with the vertical distance between the arms, which will cause an issue with both angles and the intensity of backscattered light. Another design with six arms, each with incrementally larger hanging sections was trialled to resolve this problem. A prototype of this design was produced and although theoretically sound, the required sizes of the arms and their features, proved either difficult for the 3D printer to produce with sufficient accuracy, or the PLA material the print was composed of was unable to support the weight of the arms even without a fibre collimator attached. Once a few prototypes were produced and failed to meet the robustness standards needed, this design was abandoned in lieu of a design that could withstand the stresses exerted on it by the weight of the collimators.

The final design sacrificed movable arms to focus on structural strength, as shown in figure 3.22. This design has six static arms, with channels to allow the fibre collimators to be moved along the arm. Plugs for three of the arms were also produced with M2.5 screw holes allowing compatibility with 0.5“ Thorlabs posts.

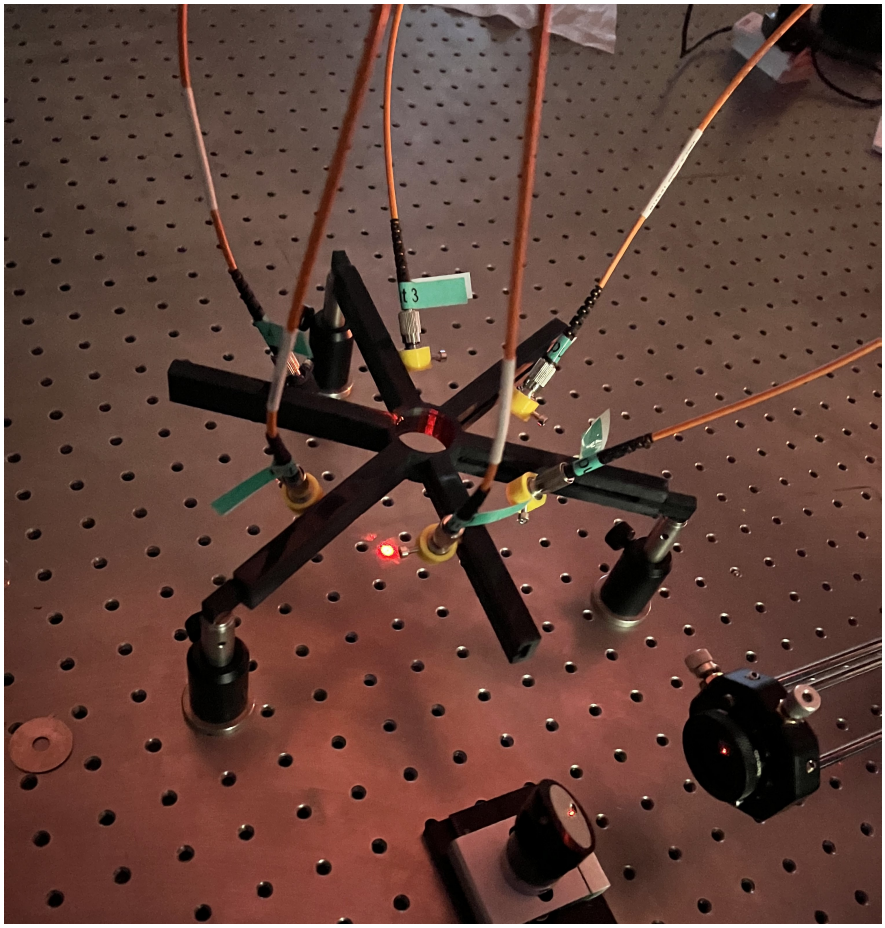

Figure 3.22: *Radial fibre holder array with focused LG beam incident on the optical bench under fibre collimator holder.*

To collect the back-scattered light and interpret it, another sub-system is needed. A set of optical fibres were chosen to transport the backscattered light. The fibres chosen were 1 metre M133L01 - Ø200 μm, 0.22 NA (Thorlabs, Inc.) to collect the light and send it to detectors. The fibres alone are poor for collecting incoming light, which given the limited amount of light returning from the system presents issues. To ensure the fibres can collect the maximum amount of light possible, a F230FC-B - 633 nm fibre collimator package (Thorlabs, Inc.) was chosen to focus incoming light onto the fibre. This package has the advantage of having a higher numerical aperture than the fibre alone. Equation 3.3 shows how numerical aperture relates the refractive index between materials and the angle between the centre of the lens and the light furthest from it. By having a numerical aperture of 0.56, the fibre collimator has a much greater area from which it can collect light. Ultimately this increases the likelihood that data can be resolved from the light backscattered

from the microfluidic device.

$$\text{Numerical Aperture, NA} = n \sin \theta \tag{3.3}$$

Once collected, the incoming intensity of the light must be converted to an equivalent voltage which is done using a silicon detector. A DET025AFC/M detector (Thorlabs, Inc.) was chosen due to its high operating frequency and low cost. Given the predicted low intensity of light that would be collected, the resulting voltage of the detector must be amplified to be reliably resolved above system noise. An AMP102 transimpedance amplifier (Thorlabs, Inc.) was selected due to its reliable compatibility with the silicon detector. The amplifier can be selected to a gain of 1, 10 or 100k which is useful given the unknown quantity of light that will reach the collimator during the experiment. To interpret the data, a National Instruments Digital Acquisition (DAQ) device is used to take all six inputs and feed them into the software. A program can then be produced in LabView to show each of the six detector outputs in a graphical format to monitor for changes.

3.3.2 Digital Holographic Microscope

In order to explore other avenues for observing blood reperfusion, another system was used to determine if a phase change could be detected whilst imaging microfluidics at short wave infrared (1550 nm) light.

The system used is a wide-field digital holographic microscope, which operates by interfering a probe beam with a reference beam to form interference patterns. By measuring this interference, object holograms can be obtained. From these holograms, intensity and phase images of the object can be reconstructed with images taken every 600 ms. This enables the imaging of empty, partially filled and full channels to be observed when liquid is driven at 1-2 Hz (frequency of human heartbeat). The full system diagram can be seen in figure 3.23.

By placing the microfluidic device on the stage above the objective lens, varying parts of the device can be investigated to observe the passage of fluid through the channels. Although other objective lenses can be used, 4x was found to clearly show junctions in the microfluidic device. This is useful for observing how the liquid splits into new channels, and if discrepancies can be identified in the case one channel does not fill correctly.

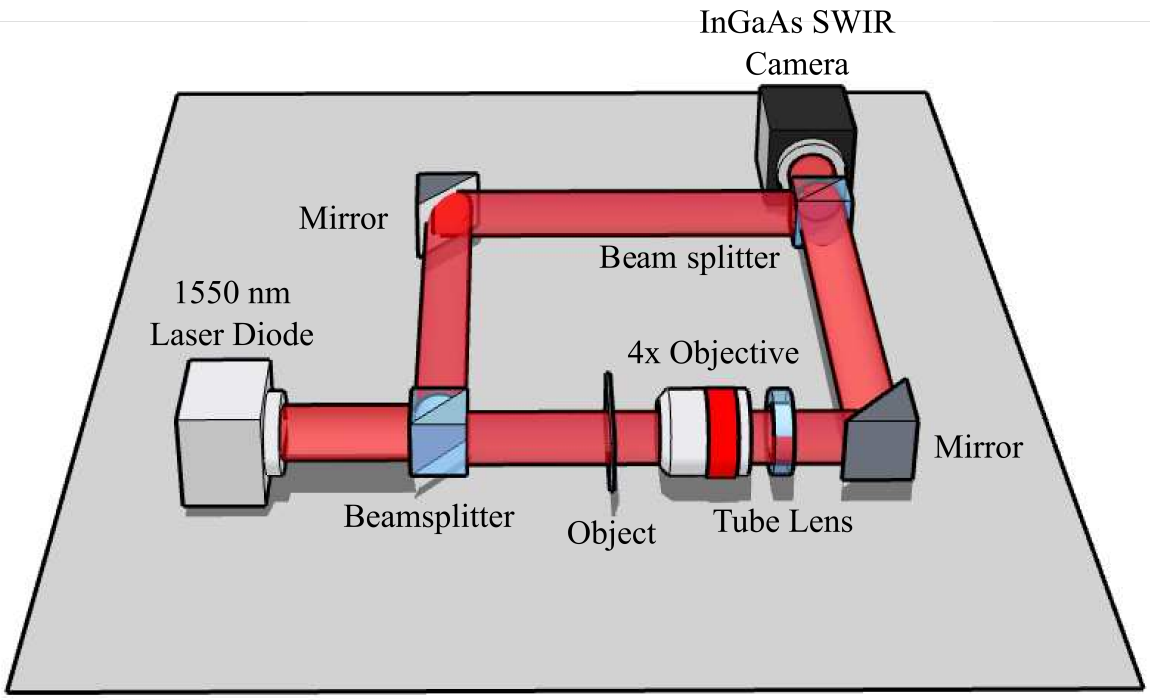

Figure 3.23: *System diagram for inverted wide-field microscope interferometer. The microscope is configured for transmission with a 4x microscope objective and 150 mm tube lens. Beam splitters are used to generate the reference and signal beams and recombine them before imaging with a camera. This system is configured for SWIR and is adopted from* Wolley et al[74].

CHAPTER 4

RESULTS AND DISCUSSION

THE methodology sections discussed the simulation methods to assess photon interaction with tissue, followed by experimental strategies. In the experimental strategies, broadly, the fabrication of microfluidic devices and optical experiments are detailed. In this chapter, the results and discussions of the outputs are covered. The results of the simulations are detailed in Section 4.1 and demonstrated outcomes as predicted from theoretical analysis and previous studies.

The fabricated microfluidic devices are discussed in section 4.2. On the optical bench, high-quality LG beams were generated, with their profiling shown in section 4.3. This system, however, did not produce any discernible data. Some possible reasons for the failure of this system are also presented in section 4.3. Finally, the use of a digital holographic microscope to determine phase change resulting from fluid reintroduction yielded excellent results, which are presented in Section 4.4.

4.1 Ray Tracing Simulation Outputs

The simulation plots the rays with a colour corresponding to the energy of the ray itself. By default, these are set in accordance with each ray's flux, i.e. red denotes 66.67% to 100% of the original ray's flux, 33.34% to 66.67% by green and the remaining by blue [75]. When the epidermis, dermis, fat and muscle are made invisible, the interaction of the rays within the tissue can be easily inspected visually.

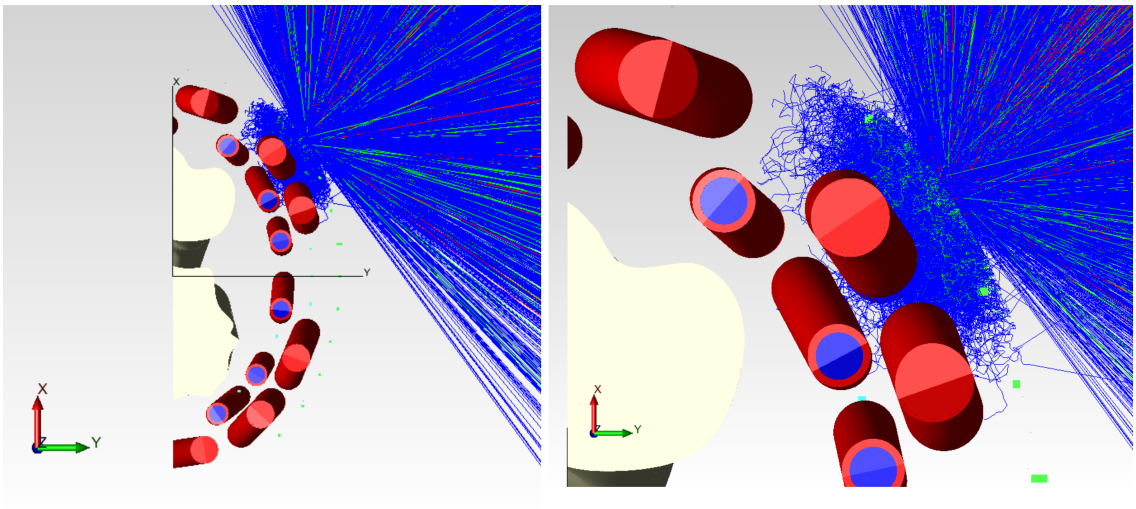

Figure 4.1: *Trace of the beam incident on forearm model with epidermis, dermis, fat and muscle removed.*

Figure 4.1 shows the beam incident on the model and the layers removed to show the light scattering as it enters the tissue. The rays are mostly scattered and absorbed from the epidermis to

the fat layer but some penetrate as far as the arteries and veins within the muscle. To carry out a more detailed analysis, the bounding spheres and internal detectors must be studied. By creating a 3D irradiance map of the spheres, the intensity and angle of back-scattered light from the model can be analysed, as shown in Figure 4.2 and 4.3.

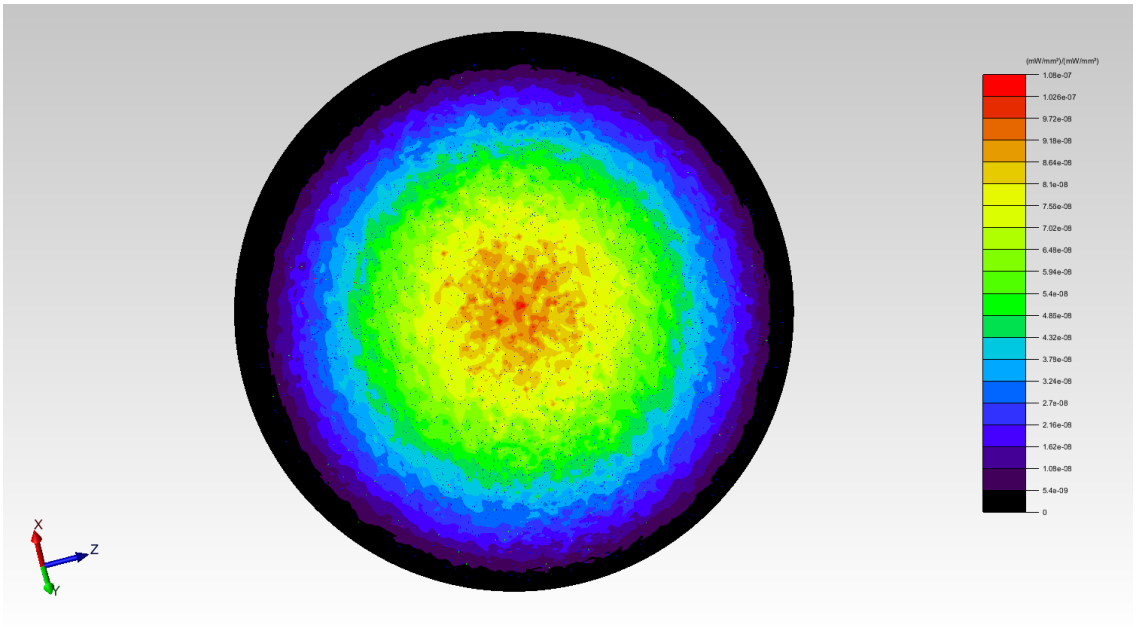

Figure 4.2: *3D irradiance maps of sphere surrounding healthy simulation model.*

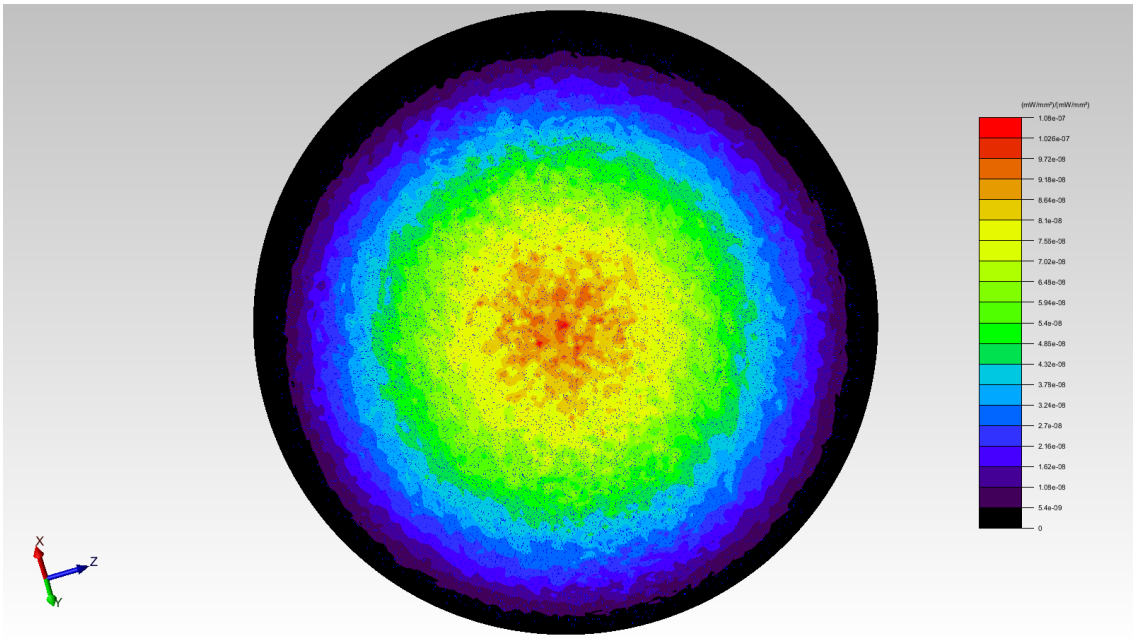

Figure 4.3: *3D irradiance maps of sphere surrounding unhealthy simulation model.*

Both spheres have almost identical irradiance profiles, which is expected given the majority of rays incident upon the spheres are either directly reflected from the epidermis or the dermis. It is

possible that with a greater number of photons (> 1 billion), any differences would be amplified. Analysis of absorption events shows a small variation in total photon count upon the sphere. The variation is small enough that the change could be caused by the anatomical variation or probabilistic outcomes based on the method used to trace the rays.

Despite back-scattered data proving inconclusive, the detectors and large vessels were compared to determine if any variations could be found. A number of dermal detector surfaces were inspected within the beam path and beyond. By doing so, changes in intensity and scattering can be observed as a result of the structural changes in the arterioles and venules within the dermis.

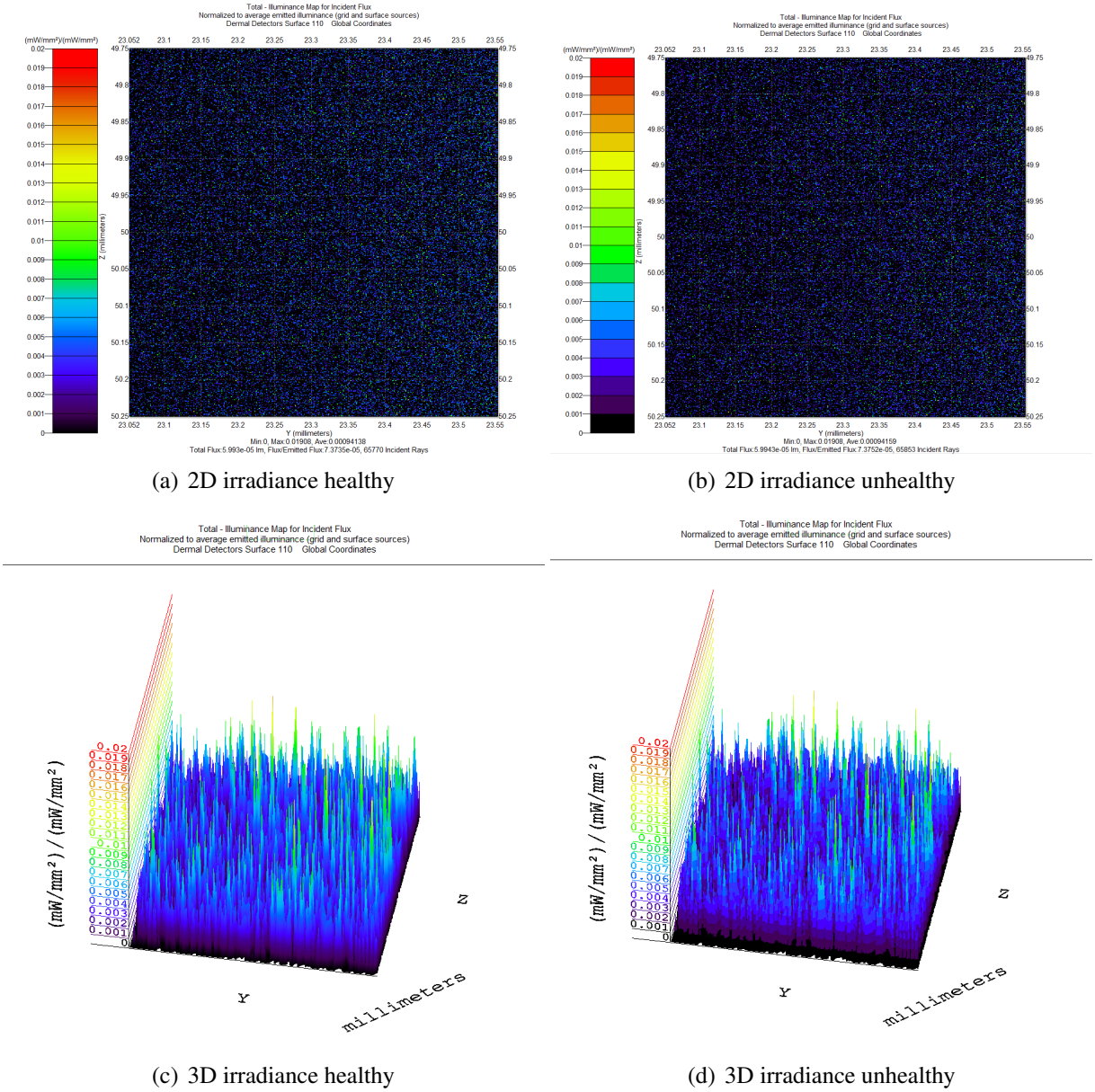

(a) 2D irradiance healthy

(b) 2D irradiance unhealthy

(c) 3D irradiance healthy

(d) 3D irradiance unhealthy

Figure 4.4: *Irradiance maps of dermal detectors within the direct path of the incident beam.*

Figure 4.4 shows the irradiance maps for a dermal detector surface on both models. For both healthy and unhealthy detectors, a large number of photons are incident on the surface. With

average intensity and incident photon count variation of less than 1%, this is statistically irrelevant. By falling directly within the beam path itself, the incident photons may have only been forward scattered a few times by the epidermis leading to the scattering that has come from variations in anatomical geometry being vastly outweighed. By measuring detector values further from the beam, any changes as a result of scattering will not be overcome by high energy forward scattered photons within the beam path itself.

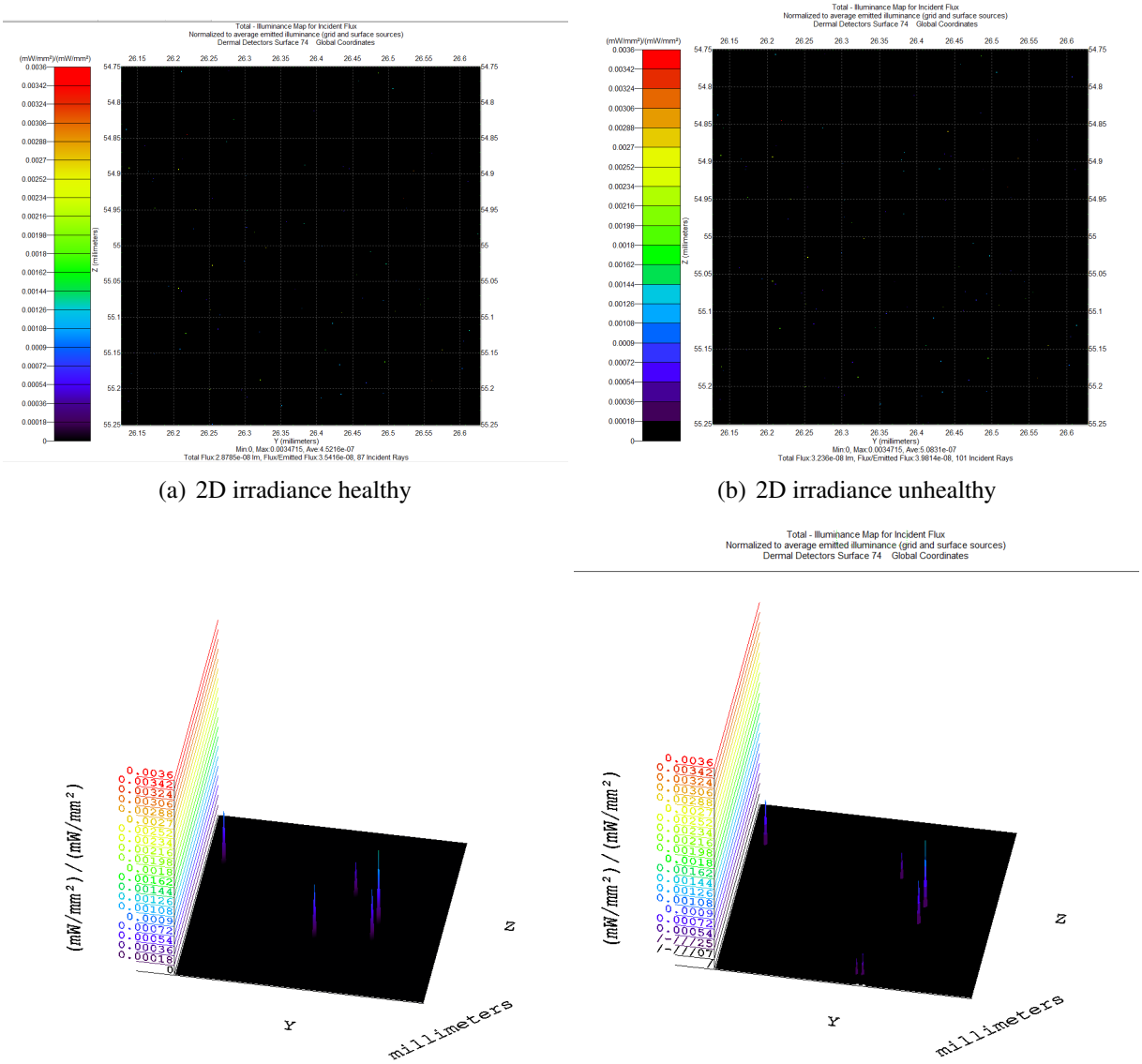

(a) 2D irradiance healthy

(b) 2D irradiance unhealthy

(c) 3D irradiance healthy

(d) 3D irradiance unhealthy

Figure 4.5: *Irradiance maps of dermal detectors outwith the direct path of the incident beam.*

When a detector is placed slightly outside of the direct beam path, there is an incident photon count reduction of over 99.9% due to the substantial forward scattering of the dermis. This does allow a far more substantial change to be seen with both average energy and incident count. In this case, the average energy difference is 11% and the incident count variation is $\approx$ 16%. These vari-

ations are substantial and suggest that when scaled to numbers of photons emitted experimentally, this level of variation should be detectable. Exiting the dermis, it was hypothesised that due to the increased tendency toward isotropic scattering, as a result of the increase in vascular wall thickness, the unhealthy model should have greater scattering which on the interior plane of the dermis would create a greater irradiance dispersion.

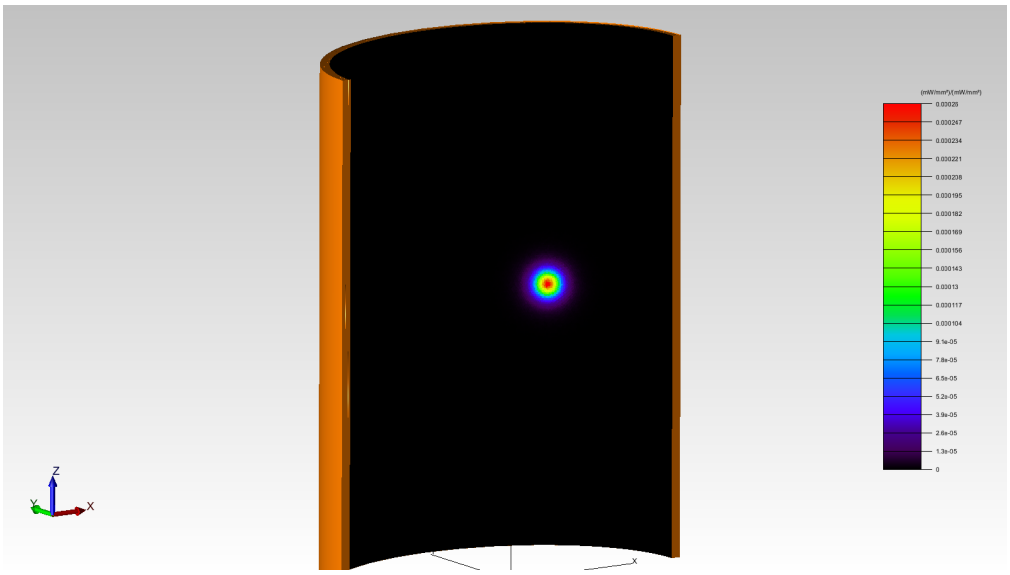

(a) Healthy model dermis

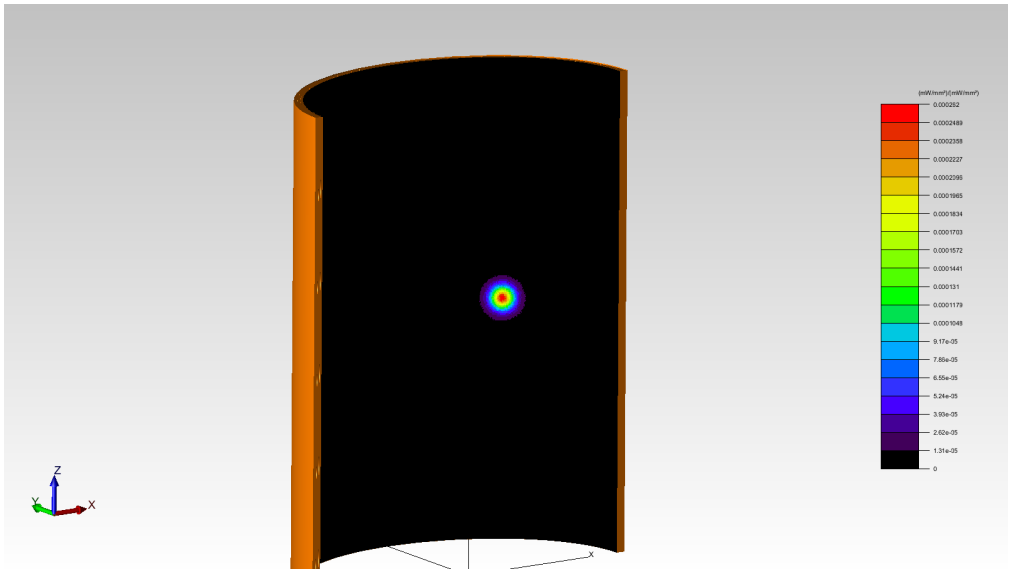

(b) Unhealthy model dermis

Figure 4.6: *Interior surface of the dermis in the healthy and unhealthy models.*

Upon observation, the unhealthy model had a maximum energy value variation of 0.7% from the healthy model with little noticeable difference in the radius of the dispersion. This was unexpected, although this may be a result of the power of the beam at the incidence overpowering that of the scattering. Due to the energy lost from multiple scattering events, the power of the incident beam

may overpower the extra scattering much like that of the dermal detector within the beam path. Due to the overall size of the venules and arterioles being very small in comparison to the amount of dermal tissue that surrounds them, the amount of variation arising from this tissue alone is likely to be insufficient to produce measurable change. However, the veins and arteries within the muscle are much larger and are likely to produce more substantial changes. Three larger vessels were analysed within the and outwith the original path of the beam shown in figure 4.7.

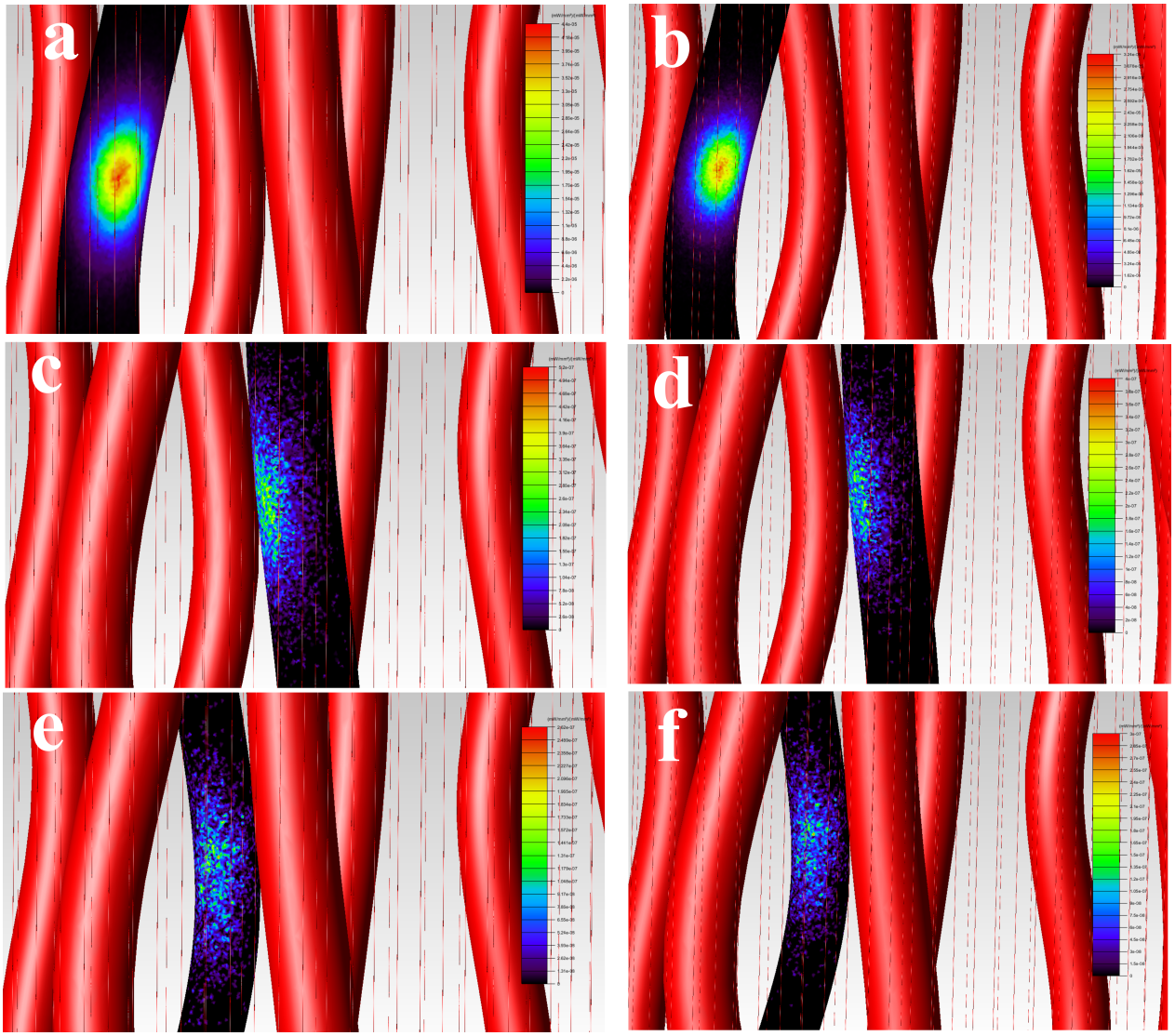

Figure 4.7: *Blood vessels at different depths shows a greater degree of scattering when comparing healthy (a,c,e) and hypertensive-prone (b,d,f) models. In the 3D model, the vessels are oriented for increasing depth from left to right.*

The variance in the results is substantial between the two models when inspecting the incidence on the vascular walls. In the first two vessels (a, c and b, d), the maximum incidence is greater with the healthy model having a 35% higher maximum value in the first vessel and an 18% increase in the second vessel. These results are in line with our expectations as the greater amount of forward scattering within the healthy model due to the greater quantity of blood allows a larger number

of energy photons to interact with the vessels in the path of the incident beam. In the deepest vessel (e, f), the opposite is the case with a higher maximum incidence on the unhealthy model. This could be due to the limited number of photons which are able to penetrate to this depth in the tissue, giving rise to seemingly larger percentage variations due to small numbers of incident events. Another possible reason could be due to the greater depth of the vessel, where the more isotropic scattering of the unhealthy tissue produced more incident events outside of the beam path itself. Scattering overall appears to be slightly greater in the hypertensive model, with the furthest extent of incident photons appearing to diverge from the centre of incidence to a larger degree. From this, we conclude that an increase in vascular wall thickness leads to a wider angle of overall scattering from the incident beam radius.

4.2 Microfluidics

The quality of the microfluidic devices produced within this study were excellent, especially given they were produced without advanced techniques. The initial attempt, which was hypothesised not to resolve fine details given a standard microfluidic procedure was used, was proven correct. However, larger details were still resolved well. The first test conducted utilised the straight channel. This was due to the difficulty in determining the quality of the plasma bonding process. Figure 4.8 shows the partial failure of the first attempt. Although the channel is still well-defined and carried the majority of the fluid, the circular sections near the inlet and outlet channels leaked. This was due to the manner in which the PDMS was cut. The outer edge of the PDMS was within 2 mm of the circular inlets, resulting in the pressure of the liquid overcoming the bond in the PDMS.

Figure 4.8: *Straight channel with failed plasma bond.*

Once an updated manufacturing procedure was determined, a more complex channel was chosen for plasma bonding. In this attempt, the cutting area was made as large as possible around the PDMS before bonding. Figure 4.9 shows a complex design following the plasma bonding process.

This device was then tested with water mixed with red food colouring to determine if the channels had bonded correctly. In figure 4.10, the channels are fully populated with liquid with no leakage into the PDMS in contact with the glass.

Figure 4.9: *First complex design produced with multiple routes for liquid to travel*

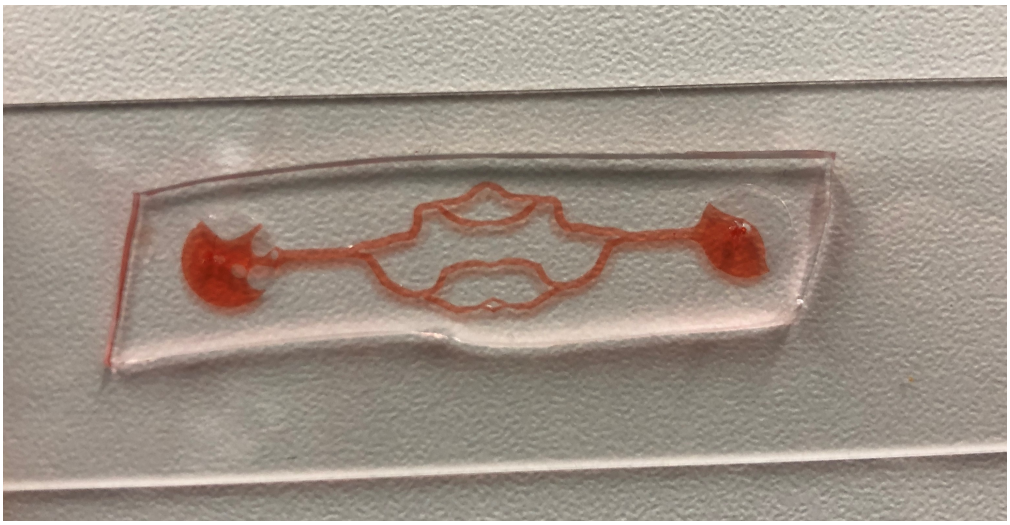

Figure 4.10: *First complex design with liquid populating all channels.*

Curiously, when testing, the reciprocating flow of fluid would tend to travel down a single avenue on any given actuation. Only when substantial pressure was applied upon forcing the liquid into the device would all channels populate. This may be due to the hydrophobic nature of the PDMS itself. Because PDMS repels water, if liquid begins to travel down one channel, any liquid following will tend to follow the path of least resistance. This results in all the liquid travelling down a single channel as shown in figure 4.11.

The main issue with this device, which leads to the inability to test with higher pressures, is the vertical dimension of the PDMS. By having such a small height, the inlet and outlet channels are

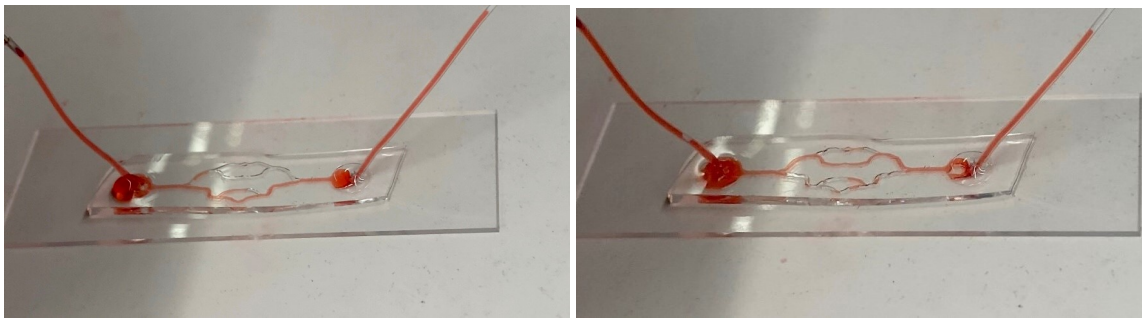

(a) Liquid in channel 1. (b) Liquid channel 2.

Figure 4.11: *Liquid travelling through microfluidic device preferentially moving down a single channel.*

small (<3 mm) which prevents the syringe tubing inserted into the channels from having enough friction to stay in place when put under a load such as that exerted by the pressure of the liquid.

4.3 Experimental Outcomes: Laguerre-Gaussian

When obtaining high-quality LG laser modes using a cylindrical lens, the incoming HG beam must be as close to ideal as possible. Beam profiling was conducted on the HG beams outputted by the laser without the cylindrical lenses' angle being changed. Figure 4.12 shows beam profiling performed on a HG_{10} laser mode. The use of this program assists with the proper alignment of the beam as it accurately defines the size and intensity of the lobes beyond the capabilities of the human eye. Poorly aligned beams may have astigmatisms, which will appear as other small peaks or one of the HG lobes will appear to be more elliptical.

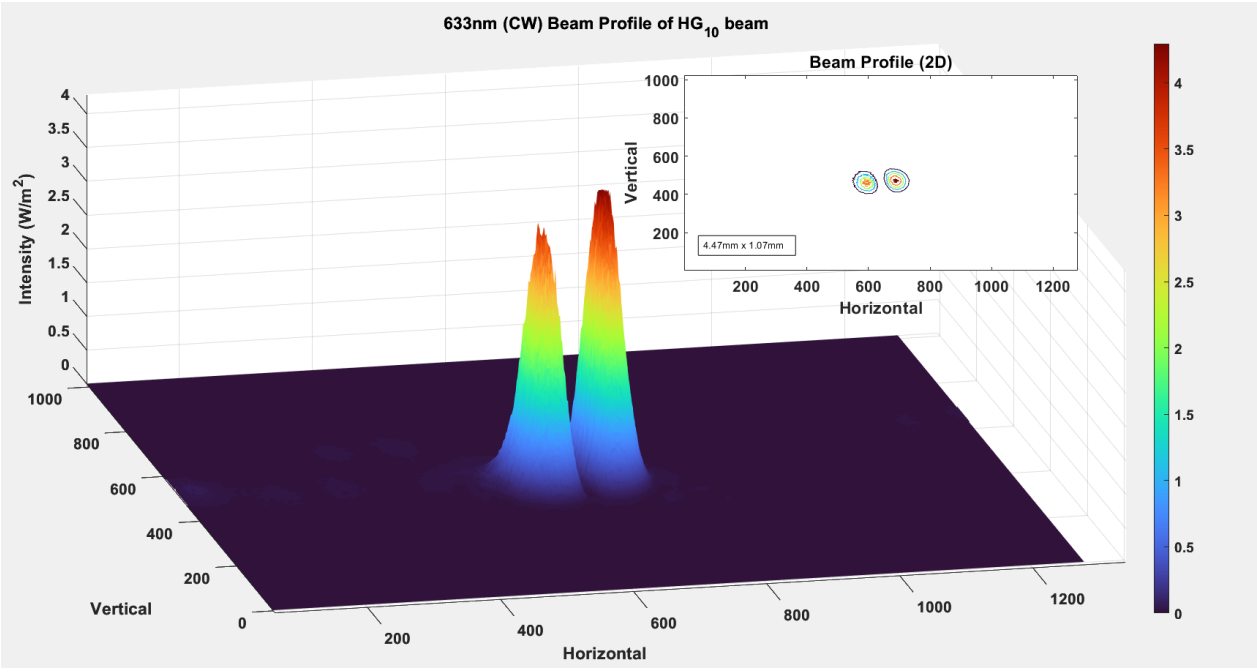

Figure 4.12: *HG_{10} laser mode profiled using an image captured on a 255 bit CMOS camera.*

Once a high-quality HG beam was produced, the rotation angle of the cylindrical lenses could be adjusted to produce an LG beam. The camera was then used to assess the quality of the LG modes, with both the phase singularity at the centre and the evenness of the helical wavefront. This also assisted in finding the ideal rotation angle of the cylindrical lenses as a seemingly complete beam can substantially reduce the intensity at certain parts of the ring. Figure 4.13 shows the variation between a properly aligned and poorly aligned LG_{01} laser mode. The desired output should have an outer edge as circular as possible with an even intensity within the ring itself and a phase singularity at the centre.

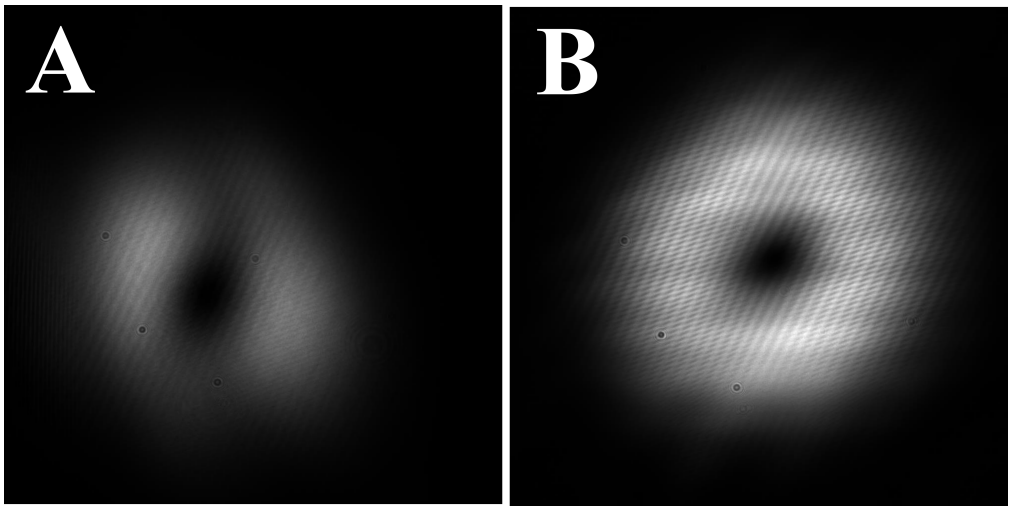

Figure 4.13: *Comparison of well-aligned and misaligned LG_{01} laser modes shown on a Thorlabs camera. Image A shows a misaligned beam and image B shows a well-aligned elliptical beam.*

To help assist with alignment, the LG beam was profiled with the results shown in figure 4.14. The beam itself has a well-defined ring and a large sharp null zone at the centre. Some minor intensity drops can be seen at two locations around the ring, which is likely caused by a slight misalignment of the cylindrical lens, however, achieving a better quality beam than this would be problematic without the use of other optical equipment.

Once the system was trialled in its completed format, there were no variations between blood being present and not. To overcome this, new detectors were used, however, ultimately the issue appears to be the amount of backscattered light received coupled with insufficient variation in the beam properties from the movement of liquid within the channels.

When considering the amount of light that reaches the collimators, some assumptions can be made to estimate incoming light. With a 5 mW input beam, if the assumption is made that only 10% of light is backscattered, the remaining light is 0.5 mW. Of this 0.5 mW it will be relatively evenly scattered in all available directions. The collimator has a diameter of 11 mm, giving an area of ≈ 95 mm^2. If the collimator is positioned 100 mm from the centre of incidence, the scattering area at this distance would be $\approx$ 62,800 mm^2. This results in an effective theoretical collection percentage of 1.515%, resulting in an incoming power to each collimator of 7.575 μW. This value

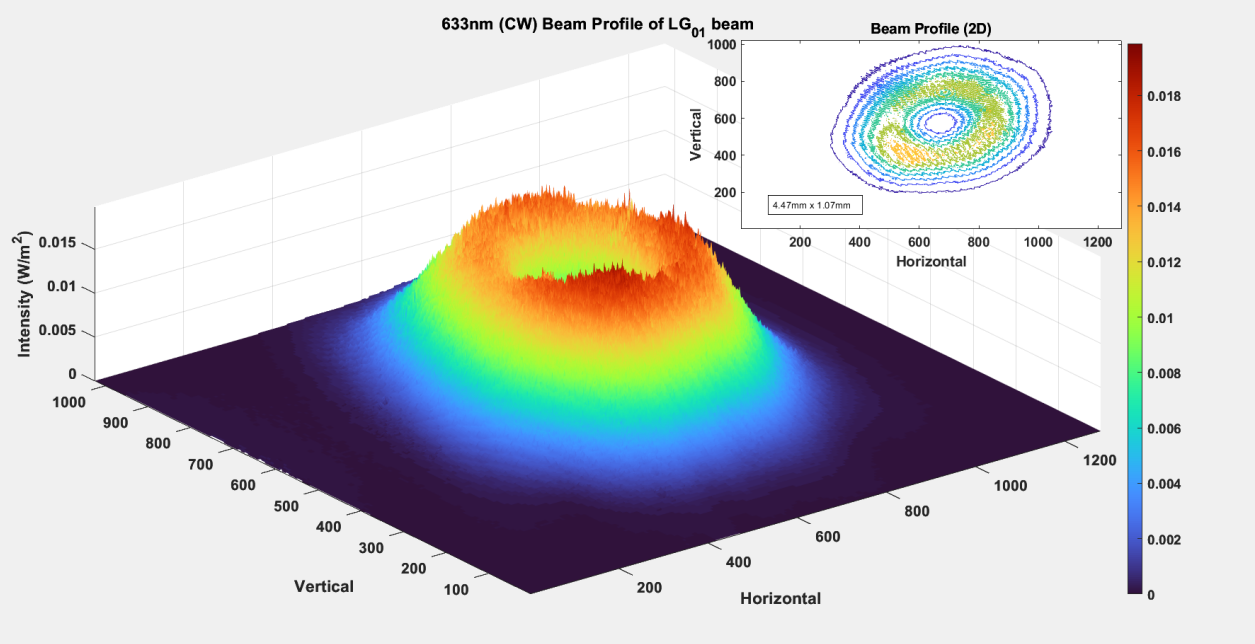

Figure 4.14: *LG_{01} beam profiled using an image captured on a 255 bit CMOS camera.*

is theoretical and represents an ideal outcome where the angle of incoming light allows adequate coupling, and that increased reflection at incidence does not result in more light scattering at an angle closer to the incident point. At this power, and given the variations in scattering produced by liquids passing through the channels, it is unsurprising the detectors could not resolve any variation.

4.4 Experimental Outcomes: Digital Holographic Microscope

The homodyne microscope was configured with an input beam at 1550 nm corresponding to short-wave infrared. Microfluidic devices were placed on the stage to observe which were suited to observe the flow. A junction point on one of the designs was chosen and phase and intensity measurements were taken as liquid moved in and out of the channels.

Figure 4.15 shows clearly the change in intensity as the fluid moves. When observing the intensity plots, the variation can best be seen when a wavefront of liquid is in the frame. This manifests as a small curved section well-defined by a low-intensity region at its edge. This results from changes in absorption and refractive index between the air and liquid. It is slightly more challenging to view a change when the vessel is completely full in comparison to its empty state. The primary change is the sharpness of the edges of the channels. When empty, the channels look more defined, likely due to the relative variation in the refractive index. PDMS has a refractive index of 1.3804 at a 10:1 mixing ratio with 10 mm thickness [76], which matches the parameters of the PDMS in the microfluidics used in the experimental setup. This value is far closer to water ($\eta = 1.33$), than air ($\eta = 1$) giving rise to far greater refraction when the vessels are empty. This can also be seen in the second image where the wavefront of the liquid is noticeably defined by a dark edge.

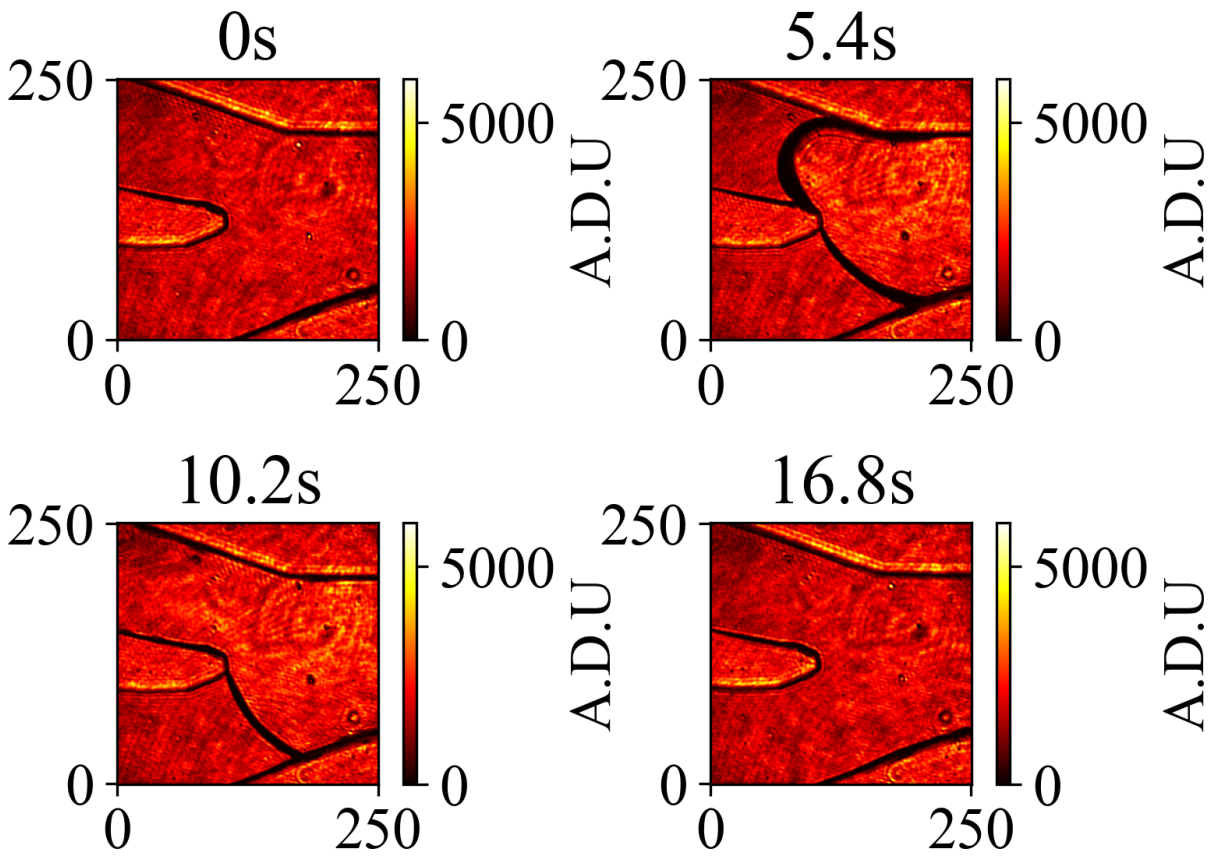

Figure 4.15: *Intensity reconstruction images from homodyne microscope showing red liquid entering a microfluidic at 1550 nm over time.*

In figure 4.16, the phase reconstruction image is shown. With no liquid, the phase variation as a function of distance is much lower than when liquid is present. This allows regions with and without liquid to be easily differentiated as opposed to using intensity alone, where only a wavefront of fluid can be easily identified. In the microfluidic shown in figure 4.9, occasionally the lower channel would not fill every time liquid entered the device as discussed in section 4.2. This is visible through observation due to the red liquid and large channel size (400 μm). However, when this may be challenging in smaller vessels, this is where phase reconstruction imaging would be useful.

Other microfluidics with smaller channel sizes ($\approx$ 40 μm) were trialled. These also produced the expected result, although the images were not as clear. This may be due to the thickness of the PDMS in this device being far greater than that shown in figure 4.10.

PDMS absorption at SWIR is relatively high regardless of thickness, but thicker PDMS will cause a substantial reduction in transmitted light in comparison to the thinner device. Between the devices, we see a 42.5% variation in the amount of transmitted light based on theoretical calculations (see Appendix C.3). Despite the issues previously noted with thin PDMS devices, in this application, they appear to be of greater use. Given the inlet channels are the main issue with these

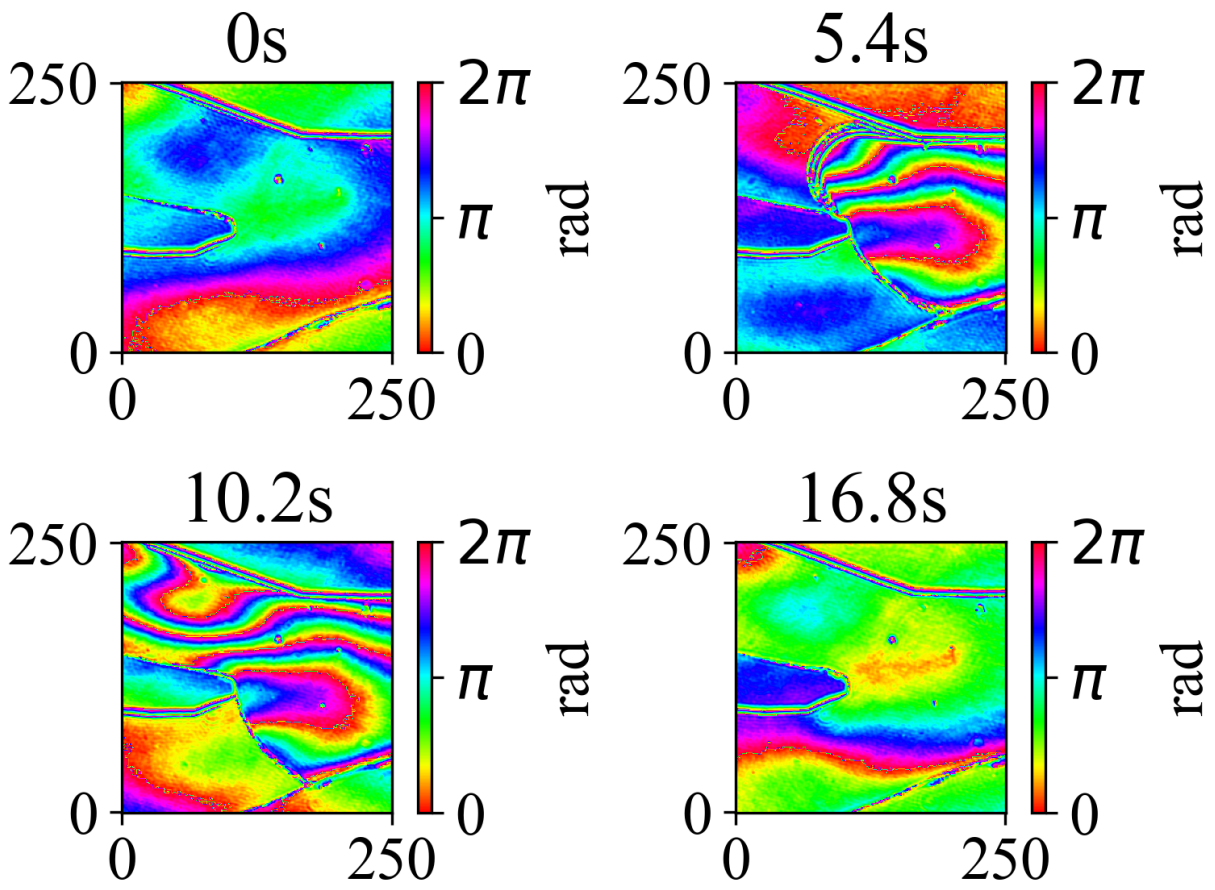

Figure 4.16: *Phase reconstruction images from a homodyne microscope showing red liquid entering a microfluidic at 1550 nm over time.*

thinner devices, in future iterations, it may be worthwhile to develop a solution for this issue. One possible method is to devise a device with horizontal inlet channels or to develop a method to allow inlet channels to be inbuilt within the device. This will be particularly useful for future work which could include the addition of artificial skin layers on top of microfluidic devices. By using horizontal channels, the entire surface of the device can be utilised without concern for access to the inlet and outlet channels.

CHAPTER 5

CONCLUSION

THE goal of this thesis was to conduct a study to explore the feasibility of using light at different wavelengths to detect changes in blood within human tissue. Enhancing the post-operative care of patients can be improved through quantitative approaches. The success of this study provides a foundation to carry out further work in this field with the eventual production of a device to be employed in a clinical setting to aid in diagnostics.

Microfluidic devices were constructed that mimic the vascular structure of human blood vessels. The creation of these devices allowed experimental testing within optical systems. The ease of producing these devices using conventional fabrication techniques provides a good platform to conduct other studies involving vascular geometries or blood flow. By providing experimental tools like these designs, the accuracy of future proof of concept studies will be greater.

Two forms of experimental optical setup were assessed for quantifying a vessel and the liquid within. It was found that using the principles of interferometry in the form of a digital holographic microscope, high-quality images in both phase and intensity could be found using short-wave infrared light. This methodology shows promising results and warrants further exploration in adapting a system operating in reflection, investigating other wavelengths and minimising size and cost.

The simulations conducted showed a substantial variation in overall light scattering within tissue as vessel geometries change. This provides the basis for conducting experimental studies to identify whether this is detectable in real human tissue. Further, it could be integrated with other measurement technologies to provide long-term post-operative monitoring or integration in consumer devices. The model produced can also be modified and used as a basis to test other hypotheses.

The positive outcomes of this study and the tools generated to aid in experimental work, provide insight into a promising future in this area of study. By building on this work, and other studies in this field, a low-cost, end-user device can be produced that will have a substantial effect on the quality of care for patients.

CHAPTER 6

FUTURE WORK

THERE are numerous avenues for future work based on the findings and tools produced during this study which would be useful for others conducting research in fields such as biophotonics, smart wearables and nanofabrication.

1. From the geometric model produced to conduct simulations in this study, simple modifications can be made to change numerous parameters within the model with relative ease. Due to the layer structure used to create the model, inclusions can be added, such as hair follicles, sweat glands and sebaceous glands. This will create more accurate models, providing more accurate results. Providing optical properties have been calculated that can be identified from the literature, any structure can be added to the forearm model. Additional wavelengths or combinations can also be tested to define ideal parameters to meet desired outcomes. If experimentally verified to be sufficiently analogous to a real forearm, the optimisation of emitters and detectors of light could be identified, giving the greatest amount of useful data to be processed by a device.

2. As computational affordability increases, these simulations will only continue to become more accurate. The primary hindrance of both the construction of the geometric model and the simulations is the ability to compute them. Even with a powerful system, there were concessions made in both the complexity of the model and the photon simulation numbers. In future studies, higher-performance machines could be used to improve accuracy, in particular, to replicate the actual geometry of the arterioles and venules, as well as including capillaries.

3. The microfluidics constructed within the study showed that vessels mimicking vascular structures could be created using standard equipment, with a high level of detail. This simple method is repeatable and can be used to create numerous devices in a single fabrication process, saving money and time. The primary issue with the devices in this study was the thickness of the PDMS. Using thin PDMS devices led to challenges in forming inlet channels that could grip syringe tubing correctly. Thicker PDMS rectifies this issue but sacrifices optical penetration. One solution to solve this for future work could be to form inlet channels horizontally instead of vertically. This would also help to mitigate pressure issues arising from the manner the liquid enters the device. Once the issues with these devices are solved there are a number of ways to modify the devices.

4. The PDMS used in microfluidic devices can be modified to introduce inclusions which will change the optical properties of the material itself. By using the correct materials, the PDMS

can be made to respond optically in a similar fashion to human skin. PDMS devices also provide an excellent platform to grow artificial tissue, creating a device with skin and underlying fluid flow. These devices can be used in a range of experiments to study blood flow within the skin. This avoids the ethical and laboratory requirements associated with working with real tissue.

5. The experimental setup using LG beams to detect blood flow changes was not successful, but there are avenues to continue to explore this area. The goal of this study was not only to prove the concept but to attempt it using simple, low-cost equipment. Future work could be to test this again with more accurate, higher-cost equipment to determine if the issue was ultimately insufficient sensitivity. This would also provide the opportunity to trial different configurations of LG beams. Although cheap and mathematically ideal, cylindrical lenses do restrict how well Laguerre-Gaussian beams can be manipulated. If an SLM or DMD is used, multiple beams with multiple modes can be used and switched very quickly.

6. The homodyne experiment showed some promising results, in imaging reperfusion through the microfluidic device. The natural next step is to implement this system in reflection to test if the results gained are still of the same quality. The camera used within the system currently is expensive due to being able to image infrared. A less expensive camera that can image red light, in order to reduce the cost of the system, could be easily implemented and should be able to achieve similar results.

REFERENCES

[1] Steven L Jacques. 'Optical properties of biological tissues: a review'. In: *Physics in Medicine Biology* 58.11 (2013), R37. URL: https://dx.doi.org/10.1088/0031-9155/58/11/R37 (cit. on pp. 6, 7, 15, 18).

[2] Mark Main et al. 'Simulated assessment of light transport through ischaemic skin flaps'. In: *British Journal of Oral and Maxillofacial Surgery* (2022) (cit. on p. 6).

[3] AC Selden. 'Photon transport parameters of diffusive media with highly anisotropic scattering'. In: *Physics in Medicine & Biology* 49.13 (2004), p. 3017 (cit. on p. 7).

[4] Steven L Jacques, CA Alter, and Scott A Prahl. 'Angular dependence of HeNe laser light scattering by human dermis'. In: *Lasers Life Sci* 1.4 (1987), pp. 309–333 (cit. on p. 7).

[5] Richard A Beth. 'Mechanical detection and measurement of the angular momentum of light'. In: *Physical Review* 50.2 (1936), p. 115 (cit. on p. 8).

[6] John David Jackson. *Classical electrodynamics*. 1999 (cit. on p. 8).

[7] L. Allen et al. 'Orbital angular momentum of light and the transformation of Laguerre-Gaussian laser modes'. In: *Phys. Rev. A* 45 (11 1992), pp. 8185–8189. URL: https://link.aps.org/doi/10.1103/PhysRevA.45.8185 (cit. on p. 8).

[8] Marco W Beijersbergen et al. 'Astigmatic laser mode converters and transfer of orbital angular momentum'. In: *Optics Communications* 96.1-3 (1993), pp. 123–132 (cit. on p. 8).

[9] Mohammad Mirhosseini et al. 'Rapid generation of light beams carrying orbital angular momentum'. In: *Optics express* 21.25 (2013), pp. 30196–30203 (cit. on p. 8).

[10] Bijun Xu et al. 'Generating an orbital-angular-momentum beam with a metasurface of gradient reflective phase'. In: *Optical Materials Express* 6.12 (2016), pp. 3940–3945 (cit. on p. 8).

[11] Xingguo Xiao et al. 'Programmable orbital angular momentum (OAM) mode multiplexer based on multi-plane light conversion (MPLC)'. In: *2018 Asia Communications and Photonics Conference (ACP)*. IEEE. 2018, pp. 1–3 (cit. on p. 8).

[12] Rui Chen et al. 'Orbital angular momentum waves: generation, detection, and emerging applications'. In: *IEEE Communications Surveys & Tutorials* 22.2 (2019), pp. 840–868 (cit. on p. 8).

[13] Ebrahim Karimi. 'Generation and manipulation of laser beams carrying orbital angular momentum for classical and quantum information applications'. PhD thesis. Università degli Studi di Napoli Federico II, 2009 (cit. on p. 8).

[14] Arthur Ashkin. 'Optical trapping and manipulation of neutral particles using lasers'. In: *Proceedings of the National Academy of Sciences* 94.10 (1997), pp. 4853–4860 (cit. on p. 9).

[15] Graham Gibson et al. 'Free-space information transfer using light beams carrying orbital angular momentum'. In: *Optics express* 12.22 (2004), pp. 5448–5456 (cit. on p. 9).

[16] A. E. Willner et al. 'Optical communications using orbital angular momentum beams'. In: *Adv. Opt. Photon.* 7.1 (2015), pp. 66–106. URL: https://opg.optica.org/aop/abstract.cfm?URI=aop-7-1-66 (cit. on p. 9).

[17] Hao Huang et al. '100 Tbit/s free-space data link enabled by three-dimensional multiplexing of orbital angular momentum, polarization, and wavelength'. In: *Optics letters* 39.2 (2014), pp. 197–200 (cit. on p. 9).

[18] Nenad Bozinovic et al. 'Terabit-Scale Orbital Angular Momentum Mode Division Multiplexing in Fibers'. In: *Science* 340.6140 (2013), pp. 1545–1548. eprint: https://www.science.org/doi/pdf/10.1126/science.1237861. URL: https://www.science.org/doi/abs/10.1126/science.1237861 (cit. on p. 9).

[19] Jonathan Leach et al. 'Measuring the Orbital Angular Momentum of a Single Photon'. In: *Phys. Rev. Lett.* 88 (25 2002), p. 257901. URL: https://link.aps.org/doi/10.1103/PhysRevLett.88.257901 (cit. on p. 9).

[20] Simon Gröblacher et al. 'Experimental quantum cryptography with qutrits'. In: *New Journal of Physics* 8.5 (2006), p. 75. URL: https://dx.doi.org/10.1088/1367-2630/8/5/075 (cit. on p. 9).

[21] Adetunmise C Dada et al. 'Experimental high-dimensional two-photon entanglement and violations of generalized Bell inequalities'. In: *Nature Physics* 7.9 (2011), pp. 677–680 (cit. on p. 9).

[22] Monika Ritsch-Marte. 'Orbital angular momentum light in microscopy'. In: *Philosophical Transactions of the Royal Society A: Mathematical, Physical and Engineering Sciences* 375.2087 (2017), p. 20150437 (cit. on p. 9).

[23] Richard Gozali et al. 'Compact OAM microscope for edge enhancement of biomedical and object samples'. In: *Review of Scientific Instruments* 88.9 (2017), p. 093701 (cit. on p. 9).

[24] Benjamin P Abbott et al. 'Observation of gravitational waves from a binary black hole merger'. In: *Physical review letters* 116.6 (2016), p. 061102 (cit. on p. 9).

[25] James Dyson. 'An interferometer microscope'. In: *Proceedings of the Royal Society of London. Series A. Mathematical and Physical Sciences* 204.1077 (1950), pp. 170–187 (cit. on p. 9).

[26] Joseph W Goodman and RW Lawrence. 'Digital image formation from electronically detected holograms'. In: *Applied physics letters* 11.3 (1967), pp. 77–79 (cit. on p. 9).

[27] Andres W Martinez et al. *Diagnostics for the developing world: microfluidic paper-based analytical devices*. 2010 (cit. on p. 9).

[28] Adelina-Gabriela Niculescu et al. 'Fabrication and applications of microfluidic devices: A review'. In: *International Journal of Molecular Sciences* 22.4 (2021), p. 2011 (cit. on p. 9).

[29] Diana Pinho et al. 'Visualization and measurements of blood cells flowing in microfluidic systems and blood rheology: A personalized medicine perspective'. In: *Journal of Personalized Medicine* 10.4 (2020), p. 249 (cit. on p. 9).

[30] Hedieh Fallahi et al. 'Flexible microfluidics: Fundamentals, recent developments, and applications'. In: *Micromachines* 10.12 (2019), p. 830 (cit. on p. 9).

[31] Marianne Fenech et al. 'Microfluidic blood vasculature replicas using backside lithography'. In: *Lab on a Chip* 19.12 (2019), pp. 2096–2106 (cit. on pp. 9, 14, 22).

[32] *Subtractive nanofabrication processes*. https://wcnt.wisc.edu/nanofabrication/processes-subtractive/. Accessed: 2022-12-31 (cit. on p. 10).

[33] *Additive nanofabrication processes*. https://wcnt.wisc.edu/nanofabrication/processes-additive/. Accessed: 2022-12-31 (cit. on p. 10).

[34] *PDMS: a review*. https://www.elveflow.com/microfluidic-reviews/general-microfluidics/the-polydimethylsiloxane-pdms-and-microfluidics/. Accessed: 2022-12-31 (cit. on p. 10).

[35] Kiran Raj M and Suman Chakraborty. 'PDMS microfluidics: A mini review'. In: *Journal of Applied Polymer Science* 137.27 (2020), p. 48958 (cit. on p. 10).

[36] Christos Markos, Kyriakos Vlachos, and George Kakarantzas. 'Guiding and thermal properties of a hybrid polymer-infused photonic crystal fiber'. In: *Optical Materials Express* 2.7 (2012), pp. 929–941 (cit. on p. 11).

[37] Jessica Godin et al. 'Microfluidics and photonics for Bio-System-on-a-Chip: A review of advancements in technology towards a microfluidic flow cytometry chip'. In: *Journal of biophotonics* 1.5 (2008), pp. 355–376 (cit. on p. 11).

[38] S Hengoju et al. 'Optofluidic detection setup for multi-parametric analysis of microbiological samples in droplets'. In: *Biomicrofluidics* 14.2 (2020), p. 024109 (cit. on p. 11).

[39] Cristina Barsanti, Francesca Lenzarini, and Claudia Kusmic. 'Diagnostic and prognostic utility of non-invasive imaging in diabetes management'. In: *World journal of diabetes* 6.6 (2015), p. 792 (cit. on p. 11).

[40] Kyeonghye Guk et al. 'Evolution of wearable devices with real-time disease monitoring for personalized healthcare'. In: *Nanomaterials* 9.6 (2019), p. 813 (cit. on p. 11).

[41] Zeineb Bouzid et al. 'Remote and wearable ECG devices with diagnostic abilities in adults: A state-of-the-science scoping review'. In: *Heart Rhythm* (2022) (cit. on p. 11).

[42] *Wearable Medical Device Market Size, Share Trends Analysis Report By Type (Diagnostic, Therapeutic), By Site (Handheld, Headband, Strap, Shoe Sensors), By Application, By Region, And Segment Forecasts, 2022 - 2030*. https://www.grandviewresearch.com/industry-analysis/wearable-medical-devices-market. Accessed: 2023-01-03 (cit. on p. 12).

[43] Tejaswini Mishra et al. 'Pre-symptomatic detection of COVID-19 from smartwatch data'. In: *Nature biomedical engineering* 4.12 (2020), pp. 1208–1220 (cit. on p. 12).

[44] Weizhuang Zhou et al. 'High-resolution digital phenotypes from consumer wearables and their applications in machine learning of cardiometabolic risk markers: Cohort Study'. In: *Journal of Medical Internet Research* 24.7 (2022), e34669 (cit. on p. 12).

[45] Jessilyn Dunn et al. 'A Method for Intelligent Allocation of Diagnostic Testing by Leveraging Data from Commercial Wearable Devices: A Case Study on COVID-19'. In: *Research Square* (2022) (cit. on p. 12).

[46] Seok Hyun Yun and Sheldon JJ Kwok. 'Light in diagnosis, therapy and surgery'. In: *Nature biomedical engineering* 1.1 (2017), pp. 1–16 (cit. on p. 12).

[47] David Huang et al. 'Optical coherence tomography'. In: *science* 254.5035 (1991), pp. 1178–1181 (cit. on p. 12).

[48] Brett E Bouma et al. 'High-resolution imaging of the human esophagus and stomach in vivo using optical coherence tomography'. In: *Gastrointestinal endoscopy* 51.4 (2000), pp. 467–474 (cit. on p. 12).

[49] Shaohua Pi et al. 'Imaging retinal structures at cellular-level resolution by visible-light optical coherence tomography'. In: *Optics letters* 45.7 (2020), pp. 2107–2110 (cit. on p. 12).

[50] Linbo Liu et al. 'Imaging the subcellular structure of human coronary atherosclerosis using micro–optical coherence tomography'. In: *Nature medicine* 17.8 (2011), pp. 1010–1014 (cit. on p. 12).

[51] David A Boas et al. *Twenty years of functional near-infrared spectroscopy: introduction for the special issue*. 2014 (cit. on p. 12).

[52] Saumya Shrivastava et al. 'A review on theranostics: an approach to targeted diagnosis and therapy'. In: *Asian Journal of Pharmaceutical Research and Development* 7.2 (2019), pp. 63–69 (cit. on p. 12).

[53] Caerwyn Ash et al. 'Effect of wavelength and beam width on penetration in light-tissue interaction using computational methods'. In: *Lasers in medical science* 32.8 (2017), pp. 1909–1918 (cit. on p. 14).

[54] *Epidermis makeup and function*. https://my.clevelandclinic.org/health/body/21901-epidermis. Accessed: 2023-01-04 (cit. on p. 14).

[55] Thomas B Fitzpatrick. 'The validity and practicality of sun-reactive skin types I through VI'. In: *Archives of dermatology* 124.6 (1988), pp. 869–871 (cit. on p. 18).

[56] Igor V Meglinski and Stephen J Matcher. 'Quantitative assessment of skin layers absorption and skin reflectance spectra simulation in the visible and near-infrared spectral regions'. In: *Physiological measurement* 23.4 (2002), p. 741 (cit. on p. 19).

[57] Gregory Altshuler, Mikhail Smirnov, and Ilya Yaroslavsky. 'Lattice of optical islets: a novel treatment modality in photomedicine'. In: *Journal of Physics D: Applied Physics* 38.15 (2005), p. 2732 (cit. on p. 19).

[58] Aletta E Karsten and Jacoba E Smit. 'Modeling and verification of melanin concentration on human skin type'. In: *Photochemistry and photobiology* 88.2 (2012), pp. 469–474 (cit. on p. 19).

[59] VV Tuchin. 'Methods and algorithms for the measurement of the optical parameters of tissues'. In: *Tissue Optics* (2007), pp. 143–192 (cit. on p. 19).

[60] Alexey N Bashkatov, Elina A Genina, and Valery V Tuchin. 'Optical properties of skin, subcutaneous, and muscle tissues: a review'. In: *Journal of Innovative Optical Health Sciences* 4.01 (2011), pp. 9–38 (cit. on p. 19).

[61] Daria K Tuchina et al. 'Quantification of glucose and glycerol diffusion in myocardium'. In: *Journal of Innovative Optical Health Sciences* 8.03 (2015), p. 1541006 (cit. on p. 19).

[62] Nadya Ugryumova, Stephen John Matcher, and Don P Attenburrow. 'Measurement of bone mineral density via light scattering'. In: *Physics in Medicine & Biology* 49.3 (2004), p. 469 (cit. on p. 19).

[63] Elina A Genina, Alexey N Bashkatov, and Valery V Tuchin. 'Optical clearing of cranial bone'. In: *Advances in Optical Technologies* 2008 (2008) (cit. on p. 19).

[64] Alexander A Oraevsky et al. 'XeCl laser ablation of atherosclerotic aorta: optical properties and energy pathways'. In: *Lasers in surgery and medicine* 12.6 (1992), pp. 585–597 (cit. on p. 19).

[65] G yoon. 'Absorption and scattering of laser light in biological media - mathematical modeling and methods for determining optical properties,' PhD thesis. Univ. of Texas at Austin, 1988 (cit. on p. 19).

[66] Anett Jannasch et al. 'Optical coherence tomography and multiphoton microscopy offer new options for the quantification of fibrotic aortic valve disease in ApoE-/- mice'. In: *Scientific reports* 11.1 (2021), pp. 1–14 (cit. on p. 19).

[67] *Optical Absorption of Hemoglobin*. https://omlc.org/spectra/hemoglobin/. Accessed: 2023-01-06 (cit. on p. 19).

[68] Dirk J Faber et al. 'Oxygen saturation-dependent absorption and scattering of blood'. In: *Physical review letters* 93.2 (2004), p. 028102 (cit. on p. 19).

[69] Andre Roggan et al. 'Optical properties of circulating human blood in the wavelength range 400-2500 nm'. In: *Journal of biomedical optics* 4.1 (1999), pp. 36–46 (cit. on p. 19).

[70] DK Sardar and LB Levy. 'Optical properties of whole blood'. In: *Lasers in medical science* 13.2 (1998), pp. 106–111 (cit. on p. 19).

[71] Bert Müller et al. 'High-resolution tomographic imaging of microvessels'. In: *Developments in X-ray Tomography VI*. Vol. 7078. SPIE. 2008, pp. 89–98 (cit. on p. 19).

[72] *SU-8 3000 Permanent Negative Epoxy Photoresist*. https://kayakuam.com/wp-content/uploads/2020/07/KAM-SU-8-3000-Datasheet-7.10-final.pdf. Accessed: 2022-11-12 (cit. on pp. 24, 26).

[73] Akhil Kallepalli and David B James. *Laser Beam Profiling: Cost-Effective Solutions*. 2053-2563. IOP Publishing, 2022. URL: https://dx.doi.org/10.1088/978-0-7503-3835-6 (cit. on pp. 35, 36).

[74] Osian Wolley et al. 'Imaging below the camera noise floor with a homodyne microscope'. In: *arXiv:2208.04898* (2022) (cit. on p. 40).

[75] *TracePro User Manual. Section 6.2*. http://45.77.157.9/CustomerSupportCenter/TraceProDownload/TracePro_User_Manual.pdf. Accessed: 2023-1-13 (cit. on p. 41).

[76] Xiaoning Zhang et al. 'Complex refractive indices measurements of polymers in visible and near-infrared bands'. In: *Applied optics* 59.8 (2020), pp. 2337–2344 (cit. on p. 51).

Appendices

A.1 Full optical properties used in simulations

Skin Type 1	Epidermis	Dermis	Fat	Homogeneous Layer	Bone	Arterioles	Venules	Artery Outer	OxyBlood	Vein Outer	DeoxyBlood
Absorption (mm-1)	1.4477767	0.029362	0.02478737	0.123	0.06	0.12075	0.12075	0.12075	0.2899	0.12075	2.609
Reduced Scattering (mm-1)	5.341	2.682	1.25	1.045	3.347	2.1045	2.1045	2.1045	2.19	2.1045	1.68
Scattering (mm-1)	29.67	26.82	5	10.45	33.47	16.188	16.188	16.188	365.87	16.188	335.76
Anisotropy	0.82	0.9	0.75	0.9	0.9	0.87	0.87	0.87	0.994	0.87	0.995
Refractive Index	1.34	1.4	1.44	1.376	1.555	1.33	1.33	1.33	1.37	1.33	1.37
Skin Type 2	Epidermis	Dermis	Fat	Homogeneous Layer	Bone	Arterioles	Venules	Artery Outer	OxyBlood	Vein Outer	DeoxyBlood
Absorption (mm-1)	5.0868704	0.029362	0.02478737	0.123	0.06	0.12075	0.12075	0.12075	0.2899	0.12075	2.609
Reduced Scattering (mm-1)	5.341	2.682	1.25	1.045	3.347	2.1045	2.1045	2.1045	2.19	2.1045	1.68
Scattering (mm-1)	29.67	26.82	5	10.45	33.47	16.188	16.188	16.188	365.87	16.188	335.76
Anisotropy	0.82	0.9	0.75	0.9	0.9	0.87	0.87	0.87	0.994	0.87	0.995
Refractive Index	1.34	1.4	1.44	1.376	1.555	1.33	1.33	1.33	1.37	1.33	1.37
Skin Type 3	Epidermis	Dermis	Fat	Homogeneous Layer	Bone	Arterioles	Venules	Artery Outer	OxyBlood	Vein Outer	DeoxyBlood
Absorption (mm-1)	11.483422	0.029362	0.02478737	0.123	0.06	0.12075	0.12075	0.12075	0.2899	0.12075	2.609
Reduced Scattering (mm-1)	5.341	2.682	1.25	1.045	3.347	2.1045	2.1045	2.1045	2.19	2.1045	1.68
Scattering (mm-1)	29.67	26.82	5	10.45	33.47	16.188	16.188	16.188	365.87	16.188	335.76
Anisotropy	0.82	0.9	0.75	0.9	0.9	0.87	0.87	0.87	0.994	0.87	0.995
Refractive Index	1.34	1.4	1.44	1.376	1.555	1.33	1.33	1.33	1.37	1.33	1.37

λ	S	Ht	F_RBC	F_Hb	γ	F_volumeFrac	u_a(skin)	u_a(melanin)	C_Blood_Dermis	u_a(Hb)	u_a(HbO2)	C_H2O_Dermis	u_a(H20)	C_Blood_Fat	C_H20_Fat
633	0.6	0.45	0.99	0.25	0.111375	0.3045	0.059668756	37.57609909	0.04	2.608	0.2899	0.6	0.0002995	0.05	0.7

Figure 1: *Optical properties calculated for 3 types of skin. The secondary table shows supplementary values used to calculate some values.*

B.2 Exposure time Calculations

MA6 operation is $18.4 mW/cm^2$ at 365 nm. $34.8 mW/cm^2$ at 405 nm.

At $18.4 mW/cm^2$ for total exposure energy of $215-240 mJ/cm^2$ a total time required is 12-13 seconds.

$$18.4 mJ/cm^2 s \times 12 = 220.8 mJ/cm^2 s$$

For SU-8 3050

$$18.4 mJ/cm^2 s \times 20 = 368 mJ/cm^2 s$$

20 seconds gives a time within the acceptable range.

C.3 Absorbance Calculations

Thick PDMS microfluidic	Thin PDMS microfluidic
$\alpha = 2.303\frac{A}{t}$	$\alpha = 2.303\frac{A}{t}$
$0.33 = 2.303\frac{A}{6.21}$	$0.33 = 2.303\frac{A}{1.79}$
$A = 0.888$	$A = 0.256$
$A = -log_{10}T$	$A = -log_{10}T$
$T = 10^{-A}$	$T = 10^{-A}$
$T = 10^{-0.888}$	$T = 10^{-0.256}$
$T = 0.129$	$T = 0.554$
$T = 12.9\%$	$T = 55.4\%$

Total Variation $= 42.5\%$ of transmitted light